Resonant inelastic x-ray scattering studies of elementary excitations

Ament, L.J.P.

Chapter 5

Orbital RIXS

5.1 Introduction

The orbital degree of freedom arises when the valence shell of an ion is not completely filled: the electrons can be distributed over the orbitals in different ways. For instance, a Ti^{3+} ion has one electron in the 3d subshell, making the ground state five-fold degenerate. It follows that orbitally active ions are also magnetic, although the converse is not necessarily true.

In many cases, the orbital degree of freedom is quenched by a large crystal field of low symmetry. In La_2CuO_4, for instance, the $x^2 - y^2$ orbital of Cu^{2+} is separated from the other $3d$ orbitals by more than 1.5 eV [70]. Transitions between those crystal field levels are called dd or crystal field excitations. The coupling of the Cu ions with their neighbors only introduces a small perturbation to this picture. Consequently, the crystal field excitations disperse only very little and are thus essentially local.

Much more interesting (from the point of view of orbital physics) are systems where the couplings between ions dominate over the local lattice coupling.

In general, orbital degeneracy can remain to very low temperatures in materials with highly symmetric lattices. In principle all local degeneracy can still be removed by the lattice through Jahn-Teller (JT) instabilities if the temperature is low enough [158, 159]. However, other interactions can dominate over the JT couplings, like superexchange (SE) interactions [24, 160–162] or relativistic spin-orbit coupling [25]. Lattice effects can then be regarded as only a perturbation to the orbital dynamics. In this chapter, we discuss the case where SE interactions dominate. Chapter 6 treats the case of dominant relativistic spin-orbit coupling.

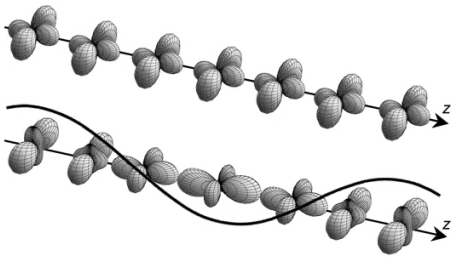

Figure 5.1: Top: a cartoon picture of an orbitally ordered ground state. Bottom: a snapshot of an orbital wave. Reprinted by permission from Macmillan Publishers Ltd: Nature **410**, 180 (2001).

When the lattice interacts strongly with the charge degree of freedom, phonons become visible in RIXS, as studied in Chapter 7.

Both the JT and SE interaction can couple neighboring orbitals and lead to orbital order. However, the excitations on top of the respective orbitally ordered ground states are very different. The lattice-dominated case yields localized dd excitations, while in SE-driven systems, collective orbital waves emerge. Fig. 5.1 shows a snapshot of such a wave, which can be crudely thought of as a dispersing dd excitation. The quanta of orbital waves are called orbitons, in analogy to spin waves and magnons.

Orbitons are a hot topic, yet they are difficult to observe in practice [163,164]. The interpretation of Raman scattering data of $LaMnO_3$ in terms of orbitons remains controversial [163,165,166]. In any case, Raman scattering is hindered by the fact that it cannot show momentum dependence, which is the distinguishing feature of a collective excitation. In contrast, RIXS has enough momentum to probe their dispersion in a large part of the Brillouin zone. Also, RIXS is directly sensitive to dipole forbidden dd excitations, unlike, for instance, optical conductivity measurements.

In section 5.2 the orbital excitations will be introduced in more detail. Also, it will be discussed how they are probed with RIXS. The remainder of the chapter describes the specific cases of 2D e_g systems like $LaMnO_3$ (section 5.3), and the t_{2g} system $YTiO_3$ (section 5.4).

5.2 Theory

Orbitally active ions can be coupled together via JT or SE interactions. In section 5.2.1 we discuss these couplings and their implications for the excitation spectrum. How the excitation spectrum of an orbitally active system is probed with RIXS is explained in section 5.2.2.

5.2.1 Orbital excitations

Superexchange is well-known to generate magnetic interactions between spins. It relies on the presence of virtual hopping processes that, on 180° bonds, promote

antiferromagnetic alignment of electron spins. In the virtual hopping processes, not only the spins of the electrons can be effectively interchanged, but also the orbitals that they occupy. These processes are described by the Kugel-Khomskii model, which can be derived by taking the low energy limit of a multi-band Hubbard model for a Mott insulator [24]. The type of orbital order promoted by SE is closely related to the magnetic order, because the hopping amplitudes depend both on the spins and orbitals involved, as stated by the Goodenough-Kanamori rules [162,167]. Fig. 5.2 shows an example of a virtual hopping process.

Kugel-Khomskii models are often frustrated because of the impossibility to optimize the superexchange bonds to a certain ion in all directions simultaneously. As a consequence, such a system often has a small orbital order parameter, or is in an orbital liquid state. In the case of an ordered ground state, a certain orbital condenses in the ground state, analogous to the Heisenberg antiferromagnet. The orbiton excitations on top of this condensate are collective, dispersing ones.

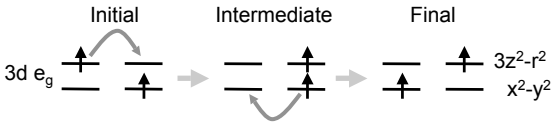

Figure 5.2: An example of a spin-orbital superexchange process on two neighboring transition metal ions with a half-filled 3d e_g subshell. The electrons usually hop via oxygen ions in between the orbitally active ions; these are omitted in the figure. The amplitude for these processes depends on the hopping integrals between the involved orbitals and the energy of the intermediate state, which involves Coulomb repulsion and Hund's rule exchange.

When JT interactions dominate over SE in orbitally active systems, the orbital dynamics are different. The lattice couples to the charge distribution of the orbitals and can mediate a cooperative JT phase transition that polarizes the orbital state. The orbital degrees of freedom are frozen out at low temperatures. Remaining degrees of freedom, *e.g.*, magnetic ones, are in a sense decoupled from the orbitals. Although the orbital pattern is fixed at low energies, the magnetic interactions are still determined by the orbital pattern, following the Goodenough-Kanamori rules [162, 167].

Orbital excitations on the JT-induced ground state are more localized in nature. Orbital excitations have to drag along lattice deformations due to the JT interaction, which reduce the orbiton band width or even localize the orbital excitations [168–170]. Another way to look at the localization is to regard the JT phonons as a bath to which the orbital degree of freedom couples. When one looks only at the orbital excitations and ignores the lattice, the orbitals constitute an open quantum system. The lattice acts as a bath and is a source of decoherence for the orbital excitations. Because of the local nature of the JT interaction, decoherence localizes the orbital excitations. In contrast, SE

interactions between orbitally active ions are not mediated by another degree of freedom, and therefore do not have this intrinsic source of decoherence.

The two types of orbital interactions suppress each other. When JT distortions are large, virtual excursions of electrons to neighboring sites are suppressed because of the large energy cost of populating excited state orbitals. Vice versa, if there are large orbital fluctuations, the slower JT distortions cannot keep up with them, and the JT energy gain is lowered.

When looking for systems that exhibit orbitons, the JT coupling needs to be small. Typically, in transition-metal oxides with octahedral symmetry, the e_g orbitals are pointing towards the negatively charged oxygen ions, so they couple stronger to the lattice than the t_{2g} orbitals. On the other side, SE interactions are enhanced near the Mott transition, *i.e.*, when the hopping parameter t is large and the Hubbard U is small. From an experimental point of view, a highly symmetric lattice signals small JT couplings. Further, structural and magnetic phase transitions can be compared: because in a JT-dominated system the spin degrees of freedom can remain active after the orbital ones have frozen out, one expects the cooperative structural phase transition and the magnetic phase transition to be at different temperatures (as in $LaMnO_3$ [168, 171]). In SE-dominated systems, the spins and orbitals are entangled and order simultaneously. In $LaTiO_3$, for instance, no separate transitions have been observed. Finally, the magnetic excitation spectrum depends on the orbital physics. When lattice distortions dominate, the orbital polarization generally induces an anisotropic magnetic SE interaction through the Goodenough-Kanamori rules. The magnetic spectra of the titanates $LaTiO_3$ and $YTiO_3$ are isotropic [160].

5.2.2 Orbital RIXS

RIXS is capable of detecting the full dynamics of orbitons. Recently, astounding progress was made in the energy and momentum resolution of RIXS, allowing, for instance, the observation of magnon excitations and their dispersions in copper oxides, see Refs. [11, 14, 53] and chapter 4. The improved resolution opens the way for probing orbitons, which are predicted to exist at similar energy scales.

Ishihara and Maekawa [66] mention three types of RIXS processes.

The first one is direct RIXS: the incident X-ray photon promotes a core electron to a certain valence orbital, and an electron from a different orbital fills the core hole.

In indirect RIXS, the core hole and photo-excited electron can affect the valence electrons in two ways: first, through the potential of the core hole and the excited electron (from hereon referred to simply as core hole potential) and second, by the Pauli exclusion principle (if the electron is excited into the valence band). These interactions lead to two indirect RIXS processes: a single-site shakeup mechanism and two-site SE bond modulation. In a single-site shakeup process, the core hole potential changes the orbit of one of the valence electrons at the core hole site. Which transitions can be effected is determined by the sym-

metry of the potential. In two-site SE bond modulation, the core hole potential influences the SE bond strength $J \sim t^2/U$ by modifying U in the intermediate state. The orbitals on the two sites involved in the bond can flip, in analogy to bimagnon RIXS at the Cu K edge. Also, the Pauli exclusion principle may play a role in SE bond modulation, in analogy to bimagnon RIXS at the Cu L edge. Of course, there are many more channels, like non-local shakeup, three-site SE modification, etc., but these are all of higher order.

Multiplet effects, like relativistic core spin-orbit coupling and intra-ionic Coulomb interactions, drive the rapid evolution of the intermediate states and so tend to wash out any particular symmetry of the core hole potential when the core hole lifetime broadening is smaller than the multiplet energy scales. Transitions of different symmetries are expected to become equal in strength. Therefore, the shakeup channel gives low energy spectra that are very similar for different edges: the differences in the initial multiplet structures are averaged out rapidly.

The effective scattering operator can in general be expanded in the number of sites involved in the scattering process:

$$\hat{O}_{\mathbf{q}} = \sum_i e^{i\mathbf{q}\cdot\mathbf{R}_i} \left(\hat{O}_i + \hat{O}_{ij} + \dots \right). \tag{5.1}$$

The phase factor comes from the dipole operators. Direct RIXS belongs to the single-site processes. Indirect RIXS contributes to both single- and two-site processes. The shakeup processes belong to the single-site part, while the SE bond modulation processes belong to the two-site part. One might think that the two-site part is a higher order correction to shakeup processes. However, since the core hole potential is averaged by multiplet effects, it is dominated by the isotropic part. The isotropic part of the potential does not contribute to on-site shakeup processes, but it does contribute to intersite bond modulation processes. It follows that it is a priori not clear which mechanism dominates indirect orbital RIXS.

One may distinguish two regimes for RIXS processes: in the first regime Γ is much larger than the relevant energy scales of the intermediate states, and these processes can be easily analyzed with the Ultra-short Core hole Lifetime expansion [48, 50], see section 2.5. In the other regime, Γ is small and its inverse is irrelevant as a cut-off time of the intermediate state dynamics. The lifetime broadening at the transition metal L edges, for instance, is relatively small, and the effects of the core hole on the valence electrons is averaged over many precessions of the core hole due to the large spin-orbit coupling in the core levels of transition metal ions.

5.3 RIXS spectra of 2D e_g systems

Published as '*Single and Double Orbital Excitations Probed by Resonant Inelastic X-ray Scattering*' in Phys. Rev. Lett. **101**, 106406 (2008) with Fiona Forte and

Jeroen van den Brink.

Abstract. *The dispersion of the elusive elementary excitations of orbital ordered systems, orbitons, has escaped detection so far. The recent advances in resonant inelastic x-ray scattering (RIXS) techniques have made it, in principle, a powerful new probe of orbiton dynamics. We compute the detailed traces that orbitons leave in RIXS for an e_g orbital ordered system, using the ultra-short core hole lifetime expansion for RIXS. We observe that both single- and double-orbiton excitations are allowed, where the former, at lower energy, have sharper features. The rich energy- and momentum-dependent intensity variations that we observe make clear that RIXS is an ideal method to identify and map out orbiton dispersions.*

5.3.1 Introduction

The exotic phases and phenomena exhibited by many transition metal oxides originate from the interplay of their electronic spin, charge and orbital degrees of freedom, coupled to the lattice dynamics [162, 172]. The orbital degree of freedom, originating from the unlifted or only partially lifted local orbital degeneracy of the $3d$ electrons, plays a particularly important role in for instance the physics of Colossal-Magneto-Resistence (CMR) manganites [24, 173, 174]. The orbitals also stand out because –in contrast to the other degrees of freedom– the dynamics of these elementary excitations is still far from being fully understood. The main reason is that it has proven very difficult to access orbital excitations experimentally.

The first claim of the observation of these elusive orbital excitations, orbitons, in $LaMnO_3$ by optical Raman scattering [163] is very controversial [165]. Irrespective of the interpretation of these data, however, a severe limitation of the Raman technique is its selectiveness to excitations carrying zero momentum. This method is thus intrinsically unsuitable to map out orbiton dispersions. Other evidence for the existence of orbital excitations comes from very recent optical pump-probe experiments on manganites [164]. Even if very ingenious, also these experiments cannot provide information on the momentum dependence of orbitons.

The success of theory in describing the dispersive magnetic RIXS data [51,52, 96] and, in particular, the success of the so-called ultra-short core hole lifetime (UCL) expansion [49, 50] provide the motivation to uncover also the signatures of orbital excitations using this theoretical framework. We therefore set out to compute and predict the detailed fingerprints of the orbitons in RIXS, finding that both single- and double-orbiton excitations are allowed, with the former having sharper features, appearing at lower energy. Orbiton scattering causes characteristic energy- and momentum-dependent intensity variations in RIXS with certain selection rules. Matrix element effects also make, for instance, the two-orbiton scattering intensity very different from the bare two-orbiton density

of states. This bolsters the case that from a theoretical perspective RIXS is ideally suited to map out the orbiton dispersions [66, 175].

In RIXS a material is resonantly excited by tuning the energy of incoming X-rays to an atomic absorption edge. In manganites, for instance, one can use the Mn K or L edge. At the Mn K edge the incoming photon promotes a 1s electron into the 4p state far above the Fermi energy, see Fig. 5.3. The present experimental resolution at the Mn edges is ~ 100 meV. In the very near future, instrumentation with an improvement with an order of magnitude in resolution at the K edge will become feasible [176], allowing the detection of low lying orbital excitations.

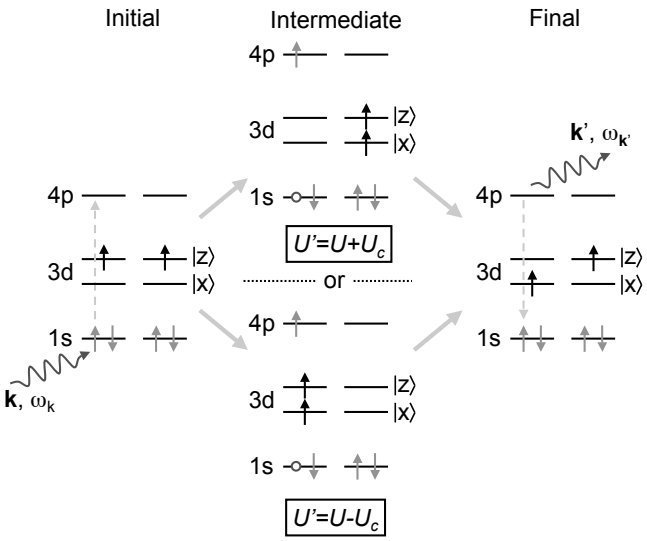

Figure 5.3: The effect of the core hole on the orbital exchange. An X-ray with energy $\hbar\omega_{\mathbf{k}}$ and momentum $\hbar\mathbf{k}$ excites the 1s electron to a 4p state. Via an intermediate state, the system reaches a final state and the core hole decays, emitting a photon of energy $\hbar\omega_{\mathbf{k}'}$ and momentum $\hbar\mathbf{k}'$. In the figure, the matrix element $\langle\downarrow_i\uparrow_j| H |\uparrow_i\uparrow_j\rangle$ is considered in presence of a core hole. There are two alternative intermediate states to reach the final state. In the upper case, the amplitude is proportional to $t^{xz}t^{xx}/(U+U_c)$ and in the lower case to $t^{xz}t^{zz}/(U-U_c)$. Adding these gives a modified exchange $J' = J\,(1+\eta)$ where η depends on U_c.

We determine the orbiton RIXS spectrum for an orbital ordered system with orbitals of e_g symmetry, but the approach that we outline can equally well be used for other orbital ordering symmetries. In order to compute the RIXS spectrum it is key to determine how the intermediate state core hole modifies the orbital-dependent superexchange processes between the $3d$ electrons. After doing so, our

calculations based on the UCL expansion will show how such modifications give rise to both single- and double-orbiton features in the RIXS spectrum. The one-orbiton part turns out to carry most spectral weight. This is in stark contrast with magnetic RIXS, where only two-magnon scattering is allowed at zero temperature [51, 52]. The computed orbiton spectrum for the e_g orbital ordering of $LaMnO_3$ shows, besides the orbiton dispersions, also strong momentum dependence of scattering intensity, with, in particular, a vanishing of it at $\mathbf{q}$=(0,0) and (π,π) for all but one orbiton branch. The orbiton is also expected to have phonon sidebands [169], observable in RIXS as well.

5.3.2 Model Hamiltonian

We focus on orbital excitations in a system with staggered e_g orbital order, such as $LaMnO_3$, the mother compound of CMR manganites. The methods used below can without restriction be applied to different orbital ordered e_g or t_{2g} systems as well. In the undoped manganite, three 3d electrons occupy the Mn t_{2g} orbitals and a fourth 3d electron can be in either one of the two Mn e_g orbitals. Below 780 K, the e_g orbitals order in an antiferro-orbital fashion. At lower temperatures, the spins order in an A-type magnetic structure, where the ferromagnetic, orbital ordered planes are stacked antiferromagnetically along the c axis [175, 177, 178].

The orbital physics of $LaMnO_3$ can be cast in a simple pseudo-spin model, where the pseudo-spin represents the Mn $3d$ e_g orbital that is occupied. It is derived starting from a generic Kondo lattice Hamiltonian [179, 180], with a local Coulomb repulsion U between the electrons in the e_g subspace. In the resulting Kugel-Khomskii model [24], the orbitals of classical antiparallel spins decouple if one neglects the Hund's rule exchange compared to the on-site Coulomb repulsion. As the quantum fluctuations associated with the large Mn core spin on the A-type AFM structure are typically small, in leading order the orbital degrees of freedom effectively decouple along the c axis, simplifying the orbital dispersion to a two-dimensional one.

The orbitals in the ab-plane are described by pseudospins, where pseudospin up corresponds to the orbital $|z\rangle \sim (3r^2-z^2)/\sqrt{6}$ and down to $|x\rangle \sim (x^2-y^2)/\sqrt{2}$. The in-plane hopping integrals are $|t^{xx}| = \frac{3}{4}t$, $|t^{zz}| = \frac{1}{4}t$ and $|t^{xz}| = \frac{\sqrt{3}}{4}t$, with reference $t = |t^{zz}|$ along the z direction. After a rotation in pseudospin space over an angle $\theta = \pi/4$, the orbital model Hamiltonian is $H^0 = \frac{J}{2}\sum_{\langle ij\rangle} H^0_{ij}$ with

$$H^0_{ij} = 3T^z_i T^z_j + T^x_i T^x_j \pm \sqrt{3}\left(T^z_i T^x_j + T^x_i T^z_j\right), \tag{5.2}$$

where $J = t^2/U$ [175]. The prefactor of the $\sqrt{3}$ term is positive in the x direction and negative in the y direction. The classical ground state has electrons alternately occupying the orbitals $\frac{1}{\sqrt{2}}(|x\rangle+|z\rangle)$ and $\frac{1}{\sqrt{2}}(|x\rangle-|z\rangle)$. We introduce sublattice A with pseudospin up and B with pseudospin down and Holstein-Primakoff bosons $T^+_{i\in A} = a_i$, $T^z_{i\in A} = 1/2 - a^\dagger_i a_i$ and $T^+_{j\in B} = a^\dagger_j$, $T^z_{j\in B} = a^\dagger_j a_j - 1/2$.

To obtain the orbital excitations we retain the terms up to quadratic order in the boson operators. After Fourier transforming the Hamiltonian and a Bogoliubov transformation, the orbiton Hamiltonian is $H^0 = \text{const.} + \sum_{\mathbf{k}} \epsilon_{\mathbf{k}} \alpha^\dagger_{\mathbf{k}} \alpha_{\mathbf{k}}$ with $\epsilon_{\mathbf{k}} = 3J\sqrt{1 + \frac{1}{6}\left(\cos k_x + \cos k_y\right)}$. The orbiton spectrum is gapped: as our orbital Hamiltonian does not have a continuous symmetry, Goldstone modes are absent.

5.3.3 Modifications by core hole

In the RIXS intermediate state, a core hole is present, and the Hamiltonian becomes $H = H^0 + H^{core}$, which includes the interaction between the core hole and the orbital degrees of freedom. The main effect of the core hole potential is to lower the Coulomb repulsion U between two e_g electrons at the core hole site by an amount U_c, disrupting the superexchange processes [52]. This effect is substantial as $U_c \approx 7$ eV [181]. To calculate the matrix elements of H^{core}, we consider how the core hole changes the superexchange processes for all different pseudospin orientations. In Fig. 5.3, the two exchange paths for the specific case $\langle{\downarrow_i\uparrow_j}| H |{\uparrow_i\uparrow_j}\rangle$ are shown. The upper process involves $t^{xz}t^{xx}/U$, where U is increased in presence of a core hole with U_c. The lower process involves $t^{xz}t^{zz}/U$ and decreases the intermediate energy U by U_c. These two processes result in

$$\begin{aligned}\langle{\downarrow\uparrow}| H^{core}_{ij} |{\uparrow\uparrow}\rangle &= 2\left(\frac{t^{xz}t^{zz}}{U-U_c} - \frac{t^{xz}t^{xx}}{U+U_c}\right)\langle{\downarrow\uparrow}| T^-_i T^z_j |{\uparrow\uparrow}\rangle \\ &= \pm\frac{\sqrt{3}}{4} J' \langle{\downarrow\uparrow}| T^-_i T^z_j |{\uparrow\uparrow}\rangle \end{aligned} \tag{5.3}$$

with $J'/J = 1 + \frac{U_c(U_c-2U)}{U^2-U_c^2}$. Note that J' is, in general, different for each matrix element. Collecting the matrix elements, one finds $H = H^0 + \frac{J}{2}\sum_{<i,j>} H^{\text{core}}_{ij} s_i s^\dagger_i$ with

$$H^{\text{core}}_{ij} = \eta_1 H^0_{ij} + \eta_2\left[\left(T^x_j - T^x_i\right) \mp \sqrt{3}\left(T^z_j - T^z_i\right)\right], \tag{5.4}$$

where s_i creates a core hole and the dimensionless coupling constants are $\eta_1 = \frac{U_c^2}{U^2-U_c^2}$ and $\eta_2 = \frac{UU_c}{U^2-U_c^2}$. The $\mp$ sign is $-$ for bonds along the x direction and $+$ along the y direction. The first term in H^{core}_{ij} is similar to the one encountered in magnetic RIXS scattering. Physically it is due to the fact that the core hole modifies the strength of the superexchange bonds to all neighboring sites. Its analytic form implies the selection rule that RIXS intensity vanishes for $\mathbf{q} = (0,0)$, as at zero momentum transfer the scattering operator is proportional to the Hamiltonian H^0 and thus commutes with it [51, 52]. The second term, with coefficient η_2, contains single orbital operators and is specific for core hole orbital coupling – in spin systems such a coupling is not allowed by conservation of S^z_{tot}. The presence of this term will allow the observation of single-orbiton scattering.

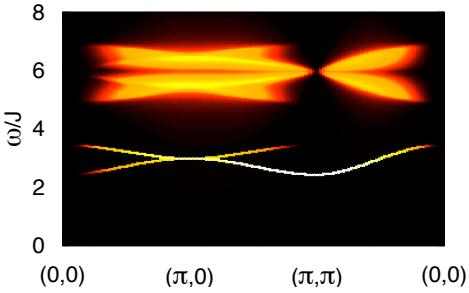

Figure 5.4: The indirect RIXS spectrum for a cut through the Brillouin zone. The lower two branches originate from single orbiton excitations, the upper, continuous spectrum from double orbiton scattering. Selection rules are such that at $\mathbf{q} = (0,0)$ all spectral weight vanishes and at $\mathbf{q} = (\pi,\pi)$ only one single-orbiton branch is active.

5.3.4 Scattering Cross section

Having derived the Hamiltonian, we can compute the RIXS spectrum using the ultra-short core hole lifetime (UCL) expansion [49,50], see section 2.5. The zeroth order term gives only elastic scattering and is thus omitted in the following. We can retain only the lowest order terms in $\eta_{1,2}J/\Gamma \approx 0.2$ in the expansion of $H^l = (H^0 + H^{\text{core}})^l$. This approximation is controlled by the large core hole broadening ($\Gamma \approx 0.58$ eV at the Mn K-edge, 1.3 eV at the Mn L_1-edge and 0.16 eV at the Mn $L_{2,3}$-edges [100]) and the values of $J \approx 25$ meV [181, 182] and $U_c/U \approx 1.1$. With this the expression for the scattering simplifies to $A_{fi} = \frac{\omega_{\text{res}}}{i\Gamma}\frac{1}{i\Gamma+\omega}\langle f|\hat{O}_{\mathbf{q}}|i\rangle$, with the effective scattering operator $\hat{O}_{\mathbf{q}} = \frac{J}{2}\sum_{<i,j>} e^{i\mathbf{q}\cdot\mathbf{R}_i} H_{ij}^{\text{core}}$. We evaluate this expression in terms of the boson creation and annihilation operators, in linear spinwave approximation. After Fourier transforming and introducing the Bogoliubov transformed orbiton operators, we obtain the single- and double-orbiton scattering operators, $\hat{O}_{\mathbf{q}}^{(1)}$ and $\hat{O}_{\mathbf{q}}^{(2)} = \sum_{\mathbf{k}} \hat{O}_{\mathbf{k},\mathbf{q}}^{(2)}$, respectively. At $T = 0$, the single-orbiton scattering operator is

$$\begin{aligned}\hat{O}_{\mathbf{q}}^{(1)} = &-\frac{\eta_1\sqrt{3N}}{8} J_{\mathbf{q}}^{-}\left(u_{\bar{\mathbf{q}}} - v_{\bar{\mathbf{q}}}\right)\alpha_{-\bar{\mathbf{q}}}^{\dagger} \\ &+ \frac{\eta_2\sqrt{N}}{4}\left(J_{\mathbf{q}} - J_{\mathbf{0}}\right)\left(u_{\mathbf{q}} - v_{\mathbf{q}}\right)\alpha_{-\mathbf{q}}^{\dagger}\end{aligned} \tag{5.5}$$

and the double orbiton scattering operator

$$\begin{aligned}\hat{O}_{\mathbf{k},\mathbf{q}}^{(2)} = &-\frac{\eta_1}{8}\left[\left(6(J_{\mathbf{q}} + J_{\mathbf{0}}) + J_{\mathbf{k}} + J_{\mathbf{k}+\mathbf{q}}\right) u_{\mathbf{k}} v_{\mathbf{k}+\mathbf{q}}\right. \\ &\left. - J_{\mathbf{k}+\mathbf{q}}\left(u_{\mathbf{k}} u_{\mathbf{k}+\mathbf{q}} + v_{\mathbf{k}} v_{\mathbf{k}+\mathbf{q}}\right)\right]\alpha_{\mathbf{k}}^{\dagger}\alpha_{-\mathbf{k}-\mathbf{q}}^{\dagger} \\ &+ \frac{\eta_2\sqrt{3}}{2} J_{\mathbf{q}}^{-} u_{\mathbf{k}} v_{\mathbf{k}+\bar{\mathbf{q}}}\alpha_{\mathbf{k}}^{\dagger}\alpha_{-\mathbf{k}-\bar{\mathbf{q}}}^{\dagger},\end{aligned} \tag{5.6}$$

where $u_{\mathbf{k}}$ and $v_{\mathbf{k}}$ are the coefficients of the Bogoliubov transformation, $\bar{\mathbf{q}} = \mathbf{q} + (\pi,\pi)$, $J_{\mathbf{k}}^{x(y)} = 2J\cos k_{x(y)}$, $J_{\mathbf{k}} = J_{\mathbf{k}}^{x} + J_{\mathbf{k}}^{y}$ and $J_{\mathbf{k}}^{-} = J_{\mathbf{k}}^{x} - J_{\mathbf{k}}^{y}$. As expected, since the z component of the total pseudospin $T_{\text{tot}}^{z} = \sum_i T_i^z$ is not conserved in the scattering process, we get a contribution to the scattering intensity both

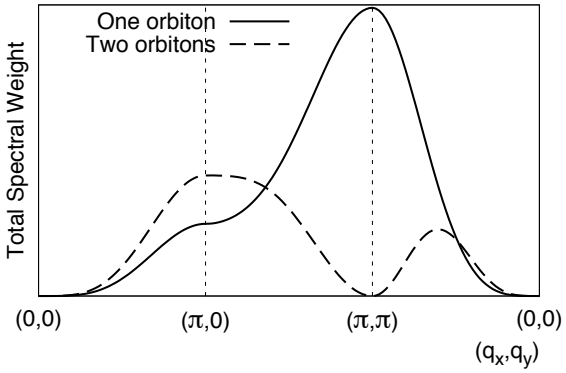

Figure 5.5: Comparison of the energy integrated spectral weight of the one- and two-orbiton RIXS spectra at fixed momentum transfer $\mathbf{q}$.

from the one- and two-orbiton part. This is a fundamental difference with respect to magnetic RIXS spectrum, where the conservation of total S^z allows only creation/annihilation of an even number of magnons [51, 52].

The resulting RIXS spectrum is shown in Fig. 5.4. We observe that the two-orbiton spectrum vanishes not only at $\mathbf{q} = (0, 0)$ but also at the antiferro-orbital ordering wavevector (π, π). This is due to the RIXS matrix elements and not to the two-orbiton DOS, which actually peaks at (π, π). The total spectral weight of the orbiton spectrum is strongly $\mathbf{q}$-dependent. In Fig. (5.5) we compare the spectral weights: the one-orbiton weight dominates and peaks at $\mathbf{q} = (\pi, \pi)$, where the two-orbiton spectrum vanishes. The two-orbiton spectrum has its maximum total weight at $(\pi, 0)$, where the total two-orbiton intensity actually outweighs the one-orbiton one. An exchange constant of $J \approx 25$ meV [181, 182] will put the two-orbiton spectrum around $\omega \approx 150$ meV. The one-orbiton peak at (π, π) is much more intense, but at $\omega \approx 2.4J \approx 60$ meV, might be more difficult to discern from the tail of the elastic peak.

5.3.5 Conclusion

Our calculations shown that in resonant inelastic X-ray experiments orbital excitations are distinguishable by characteristic variations in scattering amplitude as a function of both energy and momentum transfer. Both single- and double-orbiton excitations are allowed, with intensities that are of the same order. The single orbiton features are sharp and lower in energy; the double orbiton ones are higher in energy and more smeared out. At high symmetry points in the Brillouin zone, the intensity of specific orbiton branches vanishes. Our detailed predictions on the orbiton spectrum of an e_g orbital ordered system bolster the case that with RIXS it will for the first time be possible to directly probe orbiton dynamics and dispersions. The necessary energy and momentum resolution starts to come within reach of experiment. An observation of orbitons in RIXS will open the way to probe new orbital related quasiparticles, for instance, orbiton-magnon

bound states for which so far only theoretical evidence exists [183].

Acknowledgements. We thank Sumio Ishihara, Giniyat Khaliullin and Jan Zaanen for stimulating discussions.

5.4 RIXS spectra of $YTiO_3$

Published as '*Theory of Raman and Resonant Inelastic X-ray Scattering from Collective Orbital Excitations in $YTiO_3$*' in Phys. Rev. B **103**, 107205 (2009) with Giniyat Khaliullin.

Abstract. *We present two different theories for Raman scattering and Resonant Inelastic X-ray Scattering (RIXS) in the low temperature ferromagnetic phase of $YTiO_3$ and compare this to the available experimental data. For description of the orbital ground-state and orbital excitations, we consider two models corresponding to two theoretical limits: one where the t_{2g} orbitals are degenerate, and the other where strong lattice distortions split them. In the former model the orbitals interact through superexchange. The resulting superexchange Hamiltonian yields an orbitally ordered ground state with collective orbital excitations on top of it – the orbitons. In the orbital-lattice model, on the other hand, distortions lead to local dd-transitions between crystal field levels. Correspondingly, the orbital response functions that determine Raman and RIXS lineshapes and intensities are of cooperative or single-ion character. We find that the superexchange model yields theoretical Raman and RIXS spectra that fit very well to the experimental data.*

5.4.1 Introduction

The titanates, with a pseudo-cubic perovskite lattice structure, are good candidates to support orbitons. The Ti ions with their $3d^1$ configuration have one electron in one of the three nearly degenerate t_{2g} orbitals. Since these orbitals are directed away from the neighboring oxygen ions, the coupling to the lattice is expected to be small. Further, it has been shown that a SE-only model explains many of the ground state properties of $YTiO_3$ [184, 185]. Also, there is experimental evidence that $LaTiO_3$ is a (SE-driven) orbital liquid [186–188]. On the other hand, local crystal field models also well reproduce some of the physical properties of the titanates [189–199]. Both models have their shortcomings as well: a JT dominated description is not able to reproduce the spin wave spectrum, which is nearly isotropic in both spin and real space, while the SE model has difficulties explaining the experimentally observed orbital polarization [196–199]. Consequently, it still remains controversial which mechanism dominates the orbitals in titanates [160].

In order to resolve this controversy, it is of crucial importance to compare recent Raman and RIXS experiments on titanates [200–202] to both of the com-

peting theories. We analyze recent Raman and RIXS spectra [200–202] for $YTiO_3$ from the point of view of a SE-only model and the alternative extreme of a completely local, lattice distortion dominated model. We find that while the orbital-lattice model can be finetuned to capture some aspects of the observed spectra, the collective superexchange model yields a much better overall description of the Raman and RIXS data.

This section is organized as follows: Sec. 5.4.2 compactly reviews previous work on $YTiO_3$ and introduces the SE formalism and the local crystal field model. Sections 5.4.3 and 5.4.4 deal with the theory of Raman scattering and RIXS respectively, in both the SE and crystal field models.

5.4.2 Two models of $YTiO_3$

For the existence of collective excitations of orbitals, the so-called orbitons, it makes a difference whether the orbital order is driven by JT distortions or SE [24, 159]. For large JT distortions, the crystal field splitting is large and a local picture applies: the collective nature of the orbital excitations characteristic of orbitons is lost. In materials where the orbital-lattice coupling is small, the SE interactions between orbitals can dominate over crystal field splittings due to lattice distortions. The Ti ions have a $3d^1$ configuration, and the octahedral crystal field induces a splitting between the higher energy e_g and lower energy t_{2g} levels. Because the t_{2g} orbitals are not directed towards neighboring oxygen ions, they are not expected to couple strongly to lattice distortions.

Building on this assumption, one can derive a superexchange Hamiltonian starting from a Hubbard model. Below, we follow Refs. [184, 185] closely. By symmetry, the hopping term connects, for instance, the zx to zx and yz to yz orbitals along the z direction (c axis) via the intermediate oxygen $2p_\pi$ states. xy orbitals are not coupled along this direction. In the limit of large on-site Coulomb repulsion U, this leads to a SE interaction that depends on the spatial direction of a bond, and the resulting model is intrinsically frustrated: on any given ion, there is no orbital that minimizes the bond energy in all directions simultaneously.

Because $YTiO_3$ is ferromagnetic at low temperature ($T_c \approx 30$ K) [203], we restrict ourselves to the completely ferromagnetic part of the Hilbert space. Then one obtains the simple Hamiltonian

$$\hat{H}_0 = \frac{1}{2} J_{\mathrm{orb}} \sum_{\langle i,j \rangle} \left(\hat{A}_{ij}^{(\gamma)} + \frac{n_{\gamma,i} + n_{\gamma,j}}{2} \right), \tag{5.7}$$

with the orbital exchange integral $J_{\mathrm{orb}} = r_1 J_{SE}$, where $r_1 = 1/(1 - 3J_H/U) \approx 1.56$ parametrizing Hund's rule coupling J_H and $J_{SE} = 4t^2/U$ is the superexchange constant derived from the Hubbard model. The operator $\hat{A}_{ij}^{(\gamma)}$ depends on the direction γ of the bond ij. For example, in the z direction we have

$$\hat{A}_{ij}^{(c)} = n_{a,i} n_{a,j} + n_{b,i} n_{b,j} + a_i^\dagger b_i b_j^\dagger a_j + b_i^\dagger a_i a_j^\dagger b_j. \tag{5.8}$$

The operators $a^\dagger, b^\dagger$ and $c^\dagger$ create an electron in the yz-, zx- and xy-orbital, respectively, and $n_a = a^\dagger a$. The Hamiltonian can also be written in terms of interacting effective angular momenta $l = 1$, operating on the t_{2g} triplet. Because of the orbital frustration, these can form a myriad of different classical ground states. Refs. [184, 185] conclude that a 4-sublattice quadrupole ordered state is favored, in which the orbitals

$$|\psi_c\rangle = \frac{1}{\sqrt{3}} \left(|d_{yz}\rangle \pm |d_{zx}\rangle \pm |d_{xy}\rangle \right) \tag{5.9}$$

are condensed. The signs $\pm$ alternate between the sublattices, such that nearest-neighbor orbitals are orthogonal, supporting ferromagnetic order. On top of this condensate, two species of orbitons can be created, loosely speaking by populating either one of the two orbitals orthogonal to ψ_c. The orbiton spectrum has $3N^{1/3}$ Goldstone modes (where N is the total number of Ti ions), because the number of orbitals of a specific "color" is conserved in the plane in which it is lying. However, in $YTiO_3$ the TiO_6 octahedra are tilted. Because of this, hopping between different t_{2g} orbitals is now no longer symmetry forbidden, and the conservation of orbital "color" is violated, removing the Goldstone modes. When also some anharmonic terms of the Hamiltonian are taken into account on a mean field level, the orbiton dispersion becomes [185]

$$\begin{aligned} \omega_{1/2,\mathbf{k}} = & \sqrt{Z_\varepsilon Z_f} J_{\mathrm{orb}} \{ 1 - (1-2\varepsilon)(1-2f)(\gamma_{1,\mathbf{k}} \pm \kappa_{\mathbf{k}})^2 \\ & - 2(\varepsilon - f)(\gamma_{1,\mathbf{k}} \pm \kappa_{\mathbf{k}}) \}^{1/2}, \end{aligned} \tag{5.10}$$

where we use the signs + and − for $\omega_{1,\mathbf{k}}$ and $\omega_{2,\mathbf{k}}$ respectively. Further, $\sqrt{Z_\varepsilon Z_f} \approx 1.96$, $f \approx 0.086$, $\varepsilon \approx 0.18$, $\gamma_{1,\mathbf{k}} = (c_x + c_y + c_z)/3$ and $\kappa_{\mathbf{k}} = \sqrt{\gamma_{2,\mathbf{k}}^2 + \gamma_{2,\mathbf{k}}^2}$ with $\gamma_{2,\mathbf{k}} = \sqrt{3}(c_y - c_x)/6$ and $\gamma_{3,\mathbf{k}} = (2c_z - c_x - c_y)/6$ with $c_\alpha = \cos k_\alpha$. Eq. (5.10) describes the collective orbital modes that disperse up to energies of $2J_{\mathrm{orb}}$ and have a gap of approximately J_{orb}.

In the second orbital model for $YTiO_3$ that we consider, lattice distortions dominate over superexchange interactions. Pavarini *et al.* [190, 191] did a DMFT+LDA calculation and found that lattice distortions of the $GdFeO_3$-type lift the orbital degeneracy. They also obtained four sublattices. The resulting local eigenstates of the t_{2g} system are [191]

$$|1\rangle = 0.781\,|yz\rangle - 0.073\,|zx\rangle + 0.620\,|xy\rangle \tag{5.11}$$

$$|2\rangle = -0.571\,|yz\rangle + 0.319\,|zx\rangle + 0.757\,|xy\rangle \tag{5.12}$$

$$|3\rangle = 0.253\,|yz\rangle + 0.945\,|zx\rangle - 0.207\,|xy\rangle \tag{5.13}$$

for sublattice 1, with corresponding orbital energies $\epsilon_1 = 289$ meV, $\epsilon_2 = 488$ meV and $\epsilon_3 = 620$ meV. This yields excitation energies $\omega_1 = \epsilon_2 - \epsilon_1 = 199$ meV, $\omega_2 = \epsilon_3 - \epsilon_1 = 331$ meV. The orbital states on the other sublattices can be obtained from lattice symmetry considerations [191]. Superexchange processes

are treated as a perturbation in this model, broadening the states generated by lattice distortions. This picture is also supported by other theoretical work [189, 193, 204, 205].

It is possible to rotate the axes on each of the sublattices in such a way that in the new coordinates, the eigenstates are still given by Eqs. (5.11) through (5.13):

$$\text{subl. } 1 : (x, y, z) \mapsto (x, y, z) \tag{5.14}$$
$$\text{subl. } 2 : (x, y, z) \mapsto (y, x, z) \tag{5.15}$$
$$\text{subl. } 3 : (x, y, z) \mapsto (x, y, -z) \tag{5.16}$$
$$\text{subl. } 4 : (x, y, z) \mapsto (y, x, -z). \tag{5.17}$$

Correspondingly, the orbiton operators transform as follows:

$$\text{subl. } 1 : (a, b, c) \mapsto (a, b, c) \tag{5.18}$$
$$\text{subl. } 2 : (a, b, c) \mapsto (b, a, c) \tag{5.19}$$
$$\text{subl. } 3 : (a, b, c) \mapsto (-a, -b, c) \tag{5.20}$$
$$\text{subl. } 4 : (a, b, c) \mapsto (-b, -a, c). \tag{5.21}$$

5.4.3 Raman scattering

In the search for orbitons, Raman scattering has been an important tool for experimentalists. After the controversial first observation of orbitons in $LaMnO_3$ [163,165,166], the titanates now seem to be a more promising candidate. In addition to the reasons mentioned in previous sections, recent Raman data by Ulrich *et al.* [200] should be noted, which shows a striking temperature dependence: the spectral weight of the 235 meV peak in $YTiO_3$ increases dramatically when temperature is lowered. This can be naturally explained by collective orbitons: as temperature drops, the orbitons gain coherence and the spectral weight increases, analogous to two-magnon Raman scattering in the cuprates [206]. From the local dd-excitation point of view, temperature should not affect the intensity of local transitions between crystal field levels. Also, Ulrich *et al.* found that the polarization dependence of the spectra is hard to reconcile with the local excitation picture a result that we will reproduce below. In optical data [207], a peak is seen at the same energy and was ascribed to orbital excitations.

Earlier theoretical work on Raman scattering in the titanates [205] built on the assumption that JT-distortions determine the symmetry of the orbital order. In this paper, we investigate the Raman spectrum of $YTiO_3$ in both the lattice distortion and superexchange frameworks laid out in Sec. 5.4.2. We start out with the Loudon-Fleury effective Raman scattering operator [106, 107]

$$\hat{R} \propto \sum_{\langle i,j \rangle} (\boldsymbol{\epsilon}_i \cdot \boldsymbol{\delta}_{ij}) (\boldsymbol{\epsilon}_f \cdot \boldsymbol{\delta}_{ij}) \left(\hat{A}_{ij}^{(\gamma)} + \frac{n_{\gamma,i} + n_{\gamma,j}}{2} \right) \tag{5.22}$$

where the usual spin exchange Hamiltonian has been replaced by the orbital Hamiltonian of Eq. (5.7). $\boldsymbol{\epsilon}_{i,f}$ are the polarization vectors of the in- and outgoing light, $\boldsymbol{\delta}_{ij}$ connects nearest neighbors i and j. The physical picture is that the light induces an electric dipole transition to the intermediate state where a $3d\,t_{2g}$ electron ends up on a neighboring Ti ion, after which one of the electrons of this now doubly occupied site can hop back in another transition. In this process, the two involved electrons can end up in different orbitals, resulting in a two-orbiton excitation, in full analogy with two-magnon Raman scattering in the cuprates. As the light forces the electrons to perform a superexchange process independently of the intrinsic coupling mechanism of the orbitals, this effective Raman operator holds for the lattice distortion model too.

With this scattering operator, we calculate the Raman spectrum for the superexchange model. Similar calculations have been done before in the context of Raman scattering on orbital excitations in vanadates [208]. Adopting the geometry used in the experiment of Ref. [200], we take the polarization vectors to be in the plane parallel to the [110] and [001] directions: $\boldsymbol{\epsilon}_{i(f)} \propto (\frac{1}{\sqrt{2}}\sin\theta_{i(f)}, \frac{1}{\sqrt{2}}\sin\theta_{i(f)}, \cos\theta_{i(f)})$ where $\theta_{i(f)}$ is the angle the polarization vector makes with the c axis. Throughout this section we use a coordinate system in which the nearest neighbor Ti-Ti bonds are parallel to the coordinate axes. Substituting into Eq. (5.22) and using that $\sum_i n_{\gamma,i}$ is a conserved quantity in the superexchange model and that $\hat{H}_0\,|0\rangle \propto |0\rangle$, we find for inelastic Raman scattering

$$\hat{R} \propto \left(\cos\theta_i\cos\theta_f - \frac{1}{2}\sin\theta_i\sin\theta_f\right) \sum_{\langle i,j\rangle_c} \hat{A}_{ij}^{(c)} \tag{5.23}$$

where the sum is over bonds in the c-direction only. Performing the transformations mentioned in Sec. 5.4.2, condensing ψ_c and Fourier transforming, we obtain

$$\begin{aligned}\sum_{\langle i,j\rangle_c} \hat{A}^{(c)} =& \frac{2}{3}\sum_{\mathbf{k}} \Big[(a_{\mathbf{k}}^\dagger - b_{\mathbf{k}}^\dagger)(a_{\mathbf{k}} - b_{\mathbf{k}}) + \frac{c_z}{2}(a_{\mathbf{k}}^\dagger - b_{\mathbf{k}}^\dagger)(a_{-\mathbf{k}}^\dagger - b_{-\mathbf{k}}^\dagger) \\ &+ \frac{c_z}{2}(a_{-\mathbf{k}} - b_{-\mathbf{k}})(a_{\mathbf{k}} - b_{\mathbf{k}})\Big]\end{aligned} \tag{5.24}$$

where only quadratic terms in the operators are retained. Linear terms do not appear. Next, this result is Bogoliubov transformed according to

$$\begin{aligned}a_{\mathbf{k}} =& \; u_{\mathbf{k}}\mathrm{ch}\;\theta_{1,\mathbf{k}}\alpha_{1,\mathbf{k}} + v_{\mathbf{k}}\mathrm{ch}\;\theta_{2,\mathbf{k}}\alpha_{2,\mathbf{k}} \\ &- u_{\mathbf{k}}\mathrm{sh}\;\theta_{1,\mathbf{k}}\alpha_{1,-\mathbf{k}}^\dagger - v_{\mathbf{k}}\mathrm{sh}\;\theta_{2,\mathbf{k}}\alpha_{2,-\mathbf{k}}^\dagger,\end{aligned} \tag{5.25}$$

$$\begin{aligned}b_{\mathbf{k}} =& -v_{\mathbf{k}}\mathrm{ch}\;\theta_{1,\mathbf{k}}\alpha_{1,\mathbf{k}} + u_{\mathbf{k}}\mathrm{ch}\;\theta_{2,\mathbf{k}}\alpha_{2,\mathbf{k}} \\ &+ v_{\mathbf{k}}\mathrm{sh}\;\theta_{1,\mathbf{k}}\alpha_{1,-\mathbf{k}}^\dagger - u_{\mathbf{k}}\mathrm{sh}\;\theta_{2,\mathbf{k}}\alpha_{2,-\mathbf{k}}^\dagger,\end{aligned} \tag{5.26}$$

where the indices $1, 2$ refer to the orbiton branch. This transformation diagonalizes $\hat{H}_0$ up to quadratic order if

$$u_{\mathbf{k}} = \sqrt{\frac{1}{2} + \frac{\gamma_{2,\mathbf{k}}}{2\kappa_{\mathbf{k}}}} \tag{5.27}$$

$$v_{\mathbf{k}} = \operatorname{sign}(\gamma_{3,\mathbf{k}})\sqrt{\frac{1}{2} - \frac{\gamma_{2,\mathbf{k}}}{2\kappa_{\mathbf{k}}}} \tag{5.28}$$

$$\tanh 2\theta_{1(2),\mathbf{k}} = \gamma_{1,\mathbf{k}} \pm \kappa_{\mathbf{k}}. \tag{5.29}$$

The effective Raman scattering operator now either produces two orbitons or scatters single orbitons already present in the initial state. At zero temperature, the initial state has no orbitons (in "linear orbital wave theory", i.e. if we neglect orbiton-orbiton interactions), so we keep only the two-orbiton creation part of $\sum_{\langle i,j\rangle_c} \hat{A}^{(c)}$ in Eq. (5.24):

$$\begin{aligned}\frac{1}{3}\sum_{\mathbf{k}} \Big[&\left\{(u+v)^2(c_z \mathrm{ch}\, 2\theta_1 - \mathrm{sh}\, 2\theta_1)\right\} \alpha^\dagger_{1,\mathbf{k}}\alpha^\dagger_{1,-\mathbf{k}} \\ &+ \left\{(u-v)^2(c_z \mathrm{ch}\, 2\theta_2 - \mathrm{sh}\, 2\theta_2)\right\} \alpha^\dagger_{2,\mathbf{k}}\alpha^\dagger_{2,-\mathbf{k}} \\ &+ 2\Big\{(u^2-v^2)[\mathrm{sh}\,(\theta_1+\theta_2) - c_z \mathrm{ch}\,(\theta_1+\theta_2)]\Big\} \alpha^\dagger_{1,\mathbf{k}}\alpha^\dagger_{2,-\mathbf{k}}\Big]\end{aligned} \tag{5.30}$$

where $c_z = \cos k_z$ and the index $\mathbf{k}$ is implied on every u, v, θ_1 and θ_2.

The cross section at zero temperature now is

$$\frac{d^2\sigma}{d\omega d\Omega} \propto \sum_f \left|\langle f|\, \hat{R}\, |0\rangle\right|^2 \delta(\omega - \omega_f) \tag{5.31}$$

with f labelling the two-orbiton final states with energy ω_f. The corresponding matrix elements are given by Eq. (5.30).

Because there are orbiton-orbiton interaction terms in the Hamiltonian which are neglected in "linear orbital wave theory", we introduce a phenomenological orbiton damping of $\gamma = 30$ meV. Also, broadening from other sources such as interaction with phonons and magnons can be mimicked this way.

The result is displayed in Fig. 5.6, compared to the data from Ref. [200]. In the superexchange model, only two-orbiton creation processes contribute to the Raman spectrum. The best fit is obtained for $J_{\mathrm{orb}} = 65$ meV, close to the value estimated in Ref. [185] from magnon data of $YTiO_3$ [209]. Including orbiton-orbiton interactions will probably reduce the peak energy (in analogy to two-magnon Raman scattering), increasing the fit parameter J_{SE}.

The local model of $YTiO_3$ also yields Raman spectra via Eq. (5.22). In this model, the orbital order makes the c-direction different from the a and b ones. Therefore, all bond directions are considered separately. For technical convenience, the rotations Eqs. (5.18) through (5.21) are first performed. Bonds

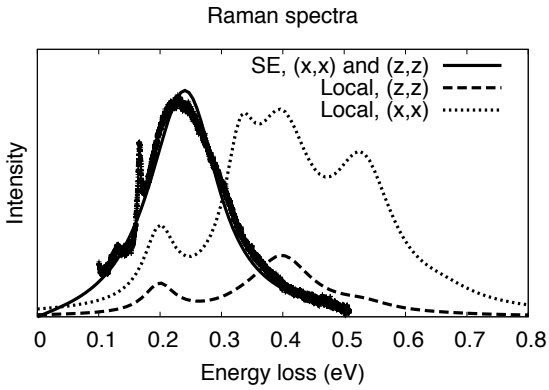

Figure 5.6: Raman spectrum of $YTiO_3$ at $T = 13$ K in (z, z) geometry, taken from Ref. [200]. A background is subtracted from the data. The sharp peak around 170 meV in the data is the two-phonon Raman signal, and is not considered in our theory. The thin-solid line is the superexchange theory curve. The anisotropy of the local model is reflected in its Raman spectra: (z, z) polarization (dashed line) gives a very different spectrum from (x, x) polarization (dotted line). In the superexchange model, the xx, yy- and zz-polarizations are equivalent. It should be noted that the experimental Raman spectra are also of cubic symmetry [200].

in the c-direction connect sublattice 1 to sublattice 3, and 2 to 4. Both these bonds give the same contribution to the Raman operator:

$$\sum_{\langle i,j\rangle_c} \left(\hat{A}_{ij}^{(c)} + \frac{1}{2}\left(n_{c,i} + n_{c,j}\right) \right) =$$
$$\sum_{\langle i,j\rangle_c} \left(n_{a,i}n_{a,j} + n_{b,i}n_{b,j} + a_i^\dagger b_i b_j^\dagger a_j + b_i^\dagger a_i a_j^\dagger b_j + \frac{1}{2}\left(n_{a,i} + n_{b,j}\right) \right). \qquad (5.32)$$

Note that the expression is symmetric in i, j. Similarly, for the a- and b-directions, we obtain again the same contribution for both bonds with $i \in$ sublattice 1 and $j \in$ sublattice 2, and for bonds with $i \in 3$ and $j \in 4$:

$$\sum_{\langle i,j\rangle_a} \left(n_{b,i}n_{a,j} + n_{c,i}n_{c,j} + b_i^\dagger c_i c_j^\dagger a_j + c_i^\dagger b_i a_j^\dagger c_j + \frac{1}{2}\left(n_{a,i} + n_{b,j}\right) \right), \qquad (5.33)$$

$$\sum_{\langle i,j\rangle_b} \left(n_{a,i}n_{b,j} + n_{c,i}n_{c,j} + a_i^\dagger c_i c_j^\dagger b_j + c_i^\dagger a_i b_j^\dagger c_j + \frac{1}{2}\left(n_{b,i} + n_{a,j}\right) \right). \qquad (5.34)$$

In general, these operators give rise to final states with one and two dd-

excitations. Using the local wave functions proposed in Ref. [204], final states with one *dd*-excitation cannot be reached in (z, z) polarization configuration, in agreement with the findings of Ref. [205]. Because the wave functions Eqs. (5.11) through (5.13) of Pavarini *et al.* are close to these states, there is little single *dd*-excitation weight (in particular in (z, z) polarization), and the spectrum is dominated by double *dd*-excitations. In the numerical calculations of the Raman spectra, the same broadening of $\gamma = 30$ meV as above is included.

The resulting Raman spectra are shown in Fig. 5.6, together with the experimental data. The experimental data peaks around 230 meV in the (z, z) polarization configuration shown here. In the experiment, other configurations give very similar line shapes, with the maximum shifting around no more than ~ 40 meV. The intensity is strongest when both in- and outgoing polarizations are directed along one of the cubic axes [200], i.e., in the zz, xx, yy polarization geometries.

Even though we have included possible orbiton-orbiton interactions only as a phenomenological damping, the superexchange model gives a very good fit to the experimental line shape: it reproduces a single peak without internal structure at approximately the right energy. The cubic isotropy of the superexchange model is in agreement with experiment, as noted in Ref. [200].

An interpretation of the Raman spectrum in terms of local crystal field excitations is problematic. Not only is the predicted strong polarization dependence of the intensity (a stark contrast between the c axis and the a, b axes) opposite of what is seen in experiment (which obeys cubic symmetry [200]), the suppression of the single dd-excitations with respect to double excitations leads to a wrong prediction of the peak energy. We tried to include corrections to the Raman operator from nondiagonal hoppings between t_{2g} orbitals but this did not improve the fit. Also, to blur the multiple peaks together into one peak, a large broadening is needed. Finally, the temperature dependence of the peak as observed in Ref. [200] is difficult to explain in the context of local dd-excitations.

5.4.4 RIXS

In the experiment [202] we analyze, the L_3 edge is used, where the 2p core electron is promoted from the spin-orbit split $j = 3/2$ state to a 3d state. The intermediate states have a complicated multiplet structure, with large spin-orbit coupling in the core levels, strong intra-ionic Coulomb interactions altered by the core potential, etc, which makes the RIXS process hard to analyze microscopically in an exact way. Fortunately, it is possible to disentangle the problem of the intermediate states from the low energy orbital transitions in the final states. Namely, since the intermediate states dynamics is much faster than that of orbital fluctuations, one can construct – based on pure symmetry grounds – a general RIXS operator describing orbital transitions between the initial and final states. In this operator, the problem of the intermediate states can be cast in the form of phenomenological matrix elements that depend only on the energy of the incident

photon and its polarization factors. These martix elements can then be calculated independently, *e.g.*, by means of well developed quantum chemistry methods on small clusters. This approach is general, but can be simplified in the (physically relevant) case where the energy dependence of martix elements is smooth: they can then be regarded as effective constants at energy scales corresponding to the low frequency orbital dynamics.

RIXS spectra are described by the Kramers-Heisenberg formula, which can be written in terms of an effective scattering operator $\hat{O}_{\mathbf{q}}$:

$$A_{fi} = \langle f| \hat{D} \frac{1}{E_i - H - i\Gamma} \hat{D} |i\rangle = \langle f| \hat{O}_{\mathbf{q}} |i\rangle \tag{5.35}$$

The cross section can be written in terms of the Green's function for the effective scattering operator:

$$\frac{d^2\sigma}{d\omega d\Omega} \propto \sum_f \left| \langle f| \hat{O}_{\mathbf{q}} |i\rangle \right|^2 \delta(\omega - \omega_{fi}) = -\frac{1}{\pi} \mathfrak{Im} \{G(\omega)\} \tag{5.36}$$

with

$$G(\omega) = -i \int_0^\infty dt e^{i\omega t} \langle i| \hat{O}^\dagger_{\mathbf{q}}(t) \hat{O}_{\mathbf{q}}(0) |i\rangle . \tag{5.37}$$

In Eq. (5.1), we neglect RIXS processes that create excitations on more than two sites in the final state, and further assume that the two-site processes are dominated by processes on nearest neighbors. Further, we assume that the titanates belong to the regime of small Γ, and that the internal dynamics of intermediate states is the fastest process in the problem. The core hole potential is then dominated by the A_{1g} component, but this only gives contributions to the Bragg peaks in the leading order (single site) of Eq. (5.1). The subleading order therefore consists of single site processes $\hat{O}_i$ of other than A_{1g} symmetries, and of two-site processes $\hat{O}_{ij}$ of A_{1g} symmetry.

The single site coupling of RIXS to the orbitals can be dubbed a "shakeup" process. If we allow the core hole potential to have a symmetry other than A_{1g}, it can locally induce an orbital flip. If the orbital ground-state is dominated by superexchange many-body interactions, a local flipped orbital will strongly interact with the neighboring sites and thus becomes a superposition of extended (multi-)orbitons. In the limit of strong crystal field splittings, however, this excitation remains a localized, on-site transition between t_{2g} levels.

Two-site processes $\hat{O}_{ij}$ may involve modulation of the superexchange bonds, analogous to two-magnon RIXS, where the superexchange constant J is effectively modified at the core hole site [10,51,52,54]. The core hole potential locally changes the Hubbard U, which in effect changes $J_{SE} = 4t^2/U$ on the Ti-Ti bonds coupled to the core hole site. Alternatively, the two-site processes can describe the lattice-mediated interaction that is altered by the presence of a core hole. The equilibrium positions and vibration frequencies of the oxygens surrounding

the core hole site may change, affecting the intersite interactions. As said above, the A_{1g} component of the core hole potential is most relevant in the two-site coupling channel $\hat{O}_{ij}$.

This section is divided into three subsections. Subsection 5.4.4 deals with the single site shakeup mechanism and contains the evaluation in the superexchange model. The next subsection, 5.4.4, is devoted to the calculation of the same processes in the local model of the orbital excitations in $YTiO_3$. The final subsection 5.4.4 covers two-site processes, evaluated within the superexchange model. A detailed comparison is made of the RIXS spectra arising from the different models.

Single site processes – Superexchange model. We start out with an analysis of the single site processes. RIXS processes that involve orbital excitations on a single site are dominated by direct transitions between the t_{2g} orbitals when the core hole potential is not of A_{1g} symmetry. In a superexchange dominated system, a local flipped orbital strongly interacts with the neighboring sites and becomes a superposition of extended orbitons.

We start from the Kramers-Heisenberg equation (2.31), where we insert the polarization-dependent dipole operator $\hat{D}$ which we take to be local: $\hat{D} = \sum_i \hat{D}_i$ with

$$\begin{aligned}\hat{D}_i = \sum_{d,m} \big(& e^{i\mathbf{k}\cdot\mathbf{R}_i} \left|m\right\rangle \left\langle m\right| \hat{\mathbf{r}} \cdot \boldsymbol{\epsilon} \left|d\right\rangle \left\langle d\right| \\ & + e^{-i\mathbf{k}'\cdot\mathbf{R}_i} \left|d\right\rangle \left\langle d\right| \hat{\mathbf{r}} \cdot \boldsymbol{\epsilon}' \left|m\right\rangle \left\langle m\right| \big) + \text{h.c.},\end{aligned} \tag{5.38}$$

where $|d\rangle$ denotes the state of atom i when it is not photo-excited and $|m\rangle$ denotes the system's intermediate eigenstates:

$$\hat{H} = \sum_m E_m \left|m\right\rangle \left\langle m\right|. \tag{5.39}$$

Now we consider only the single site part of the effective scattering operator in Eq. (5.1):

$$\hat{O}_i = \sum_{d,d',m} \left|d'\right\rangle \left\langle d'\right| \hat{\mathbf{r}}' \cdot \boldsymbol{\epsilon}' \left|m\right\rangle \frac{1}{E_i - E_m - i\Gamma} \left\langle m\right| \boldsymbol{\epsilon} \cdot \hat{\mathbf{r}} \left|d\right\rangle \left\langle d\right| \tag{5.40}$$

Next we decompose the operator part into terms transforming according to the rows of the irreducible representations of the octahedral group (labeled by Γ, not to be confused with the core hole lifetime broadening):

$$\left|d'\right\rangle \left\langle d\right| = \sum_{\Gamma} \Gamma_{d'd} \hat{\Gamma}. \tag{5.41}$$

In the second quantized picture, we need only terms that are quadratic in the creation and annihilation operators. With the irreducible representations

A_{1g}, T_{1u}, E_g and T_{2g} all possible $|d'\rangle\langle d|$ can be constructed. Therefore $\hat{\Gamma}$ assumes only the following forms:

$$A_{1g} : \hat{\Gamma} = 1 \tag{5.42}$$

$$T_{1u} : \hat{\Gamma} \in \{\hat{l}_x, \hat{l}_y, \hat{l}_z, \} \tag{5.43}$$

$$E_g : \hat{\Gamma} \in \{\hat{Q}_x, \hat{Q}_z\} \tag{5.44}$$

$$T_{2g} : \hat{\Gamma} \in \{\hat{T}_x, \hat{T}_y, \hat{T}_z\}. \tag{5.45}$$

The operators $\hat{\Gamma}$ and the corresponding 3×3 matrices $\Gamma_{d'd}$ are defined in Appendix B.1. Because A_{1g} only contributes to elastic scattering, we drop it from hereon.

Further, we also decompose the dipole matrix elements into

$$\langle d'|\,\hat{\beta}\,|m\rangle\langle m|\,\hat{\alpha}\,|d\rangle = \sum_{\Gamma} \Gamma_{\beta\alpha} M^{\Gamma}_{d'd} \tag{5.46}$$

with $\hat{\alpha}, \hat{\beta} \in \{\hat{x}, \hat{y}, \hat{z}\}$ and the $M^{\Gamma}_{d'd}$ listed in Appendix B.2: Eqs. (B.10) through (B.18). Plugging Eqs. (5.41) and (5.46) into Eq. (5.40), we obtain

$$\hat{O}_i = \sum_{d,d',m} \sum_{\Gamma'} \sum_{\alpha,\beta} \frac{\epsilon'_\beta \epsilon_\alpha \Gamma'_{\beta\alpha} M^{\Gamma'}_{d'd}}{E_i - E_m - i\Gamma} \sum_{\Gamma} \Gamma_{d'd} \hat{\Gamma}_i \tag{5.47}$$

which can be simplified using

$$\sum_{d,d'} M^{\Gamma'}_{d'd} \Gamma_{d'd} = \delta_{\Gamma,\Gamma'} \sum_{d,d'} M^{\Gamma}_{d'd} \Gamma_{d'd}. \tag{5.48}$$

This identity can be proven by interpreting M^{Γ} and Γ as matrices indexed by d and d'. Then it can be seen that $M^{\Gamma} \propto \Gamma$. We thus obtain

$$\sum_{d,d'} M^{\Gamma'}_{d'd} \Gamma_{d'd} = \mathrm{Tr}\left(M^{\Gamma'} \Gamma^T\right) \propto \mathrm{Tr}\left(\Gamma' \Gamma^T\right) \tag{5.49}$$

which is zero for $\Gamma \neq \Gamma'$, proving the above identity. We find then

$$\hat{O}_i = \sum_{\Gamma} P_\Gamma \mathcal{M}_\Gamma \hat{\Gamma}_i \tag{5.50}$$

with a polarization factor

$$P_\Gamma = \sum_{\alpha,\beta} \epsilon'_\beta \Gamma_{\beta\alpha} \epsilon_\alpha \tag{5.51}$$

and the matrix elements $\mathcal{M}_\Gamma$ depending on the multiplet effects in the intermediate state

$$\mathcal{M}_\Gamma = \sum_{d,d',m} \frac{M^{\Gamma}_{d'd} \Gamma_{d'd}}{E_i - E_m - i\Gamma}\ . \tag{5.52}$$

One can perform the sum over m, which yields

$$\sum_m \frac{M^{Q_x}_{d'd}}{E_i - E_m - i\Gamma} = \langle d'| \left(\hat{y} \frac{1}{E_i - H - i\Gamma} \hat{y} - \hat{x} \frac{1}{E_i - H - i\Gamma} \hat{x} \right) |d\rangle \tag{5.53}$$

and similar expressions for the other representations. As discussed above, we will assume that the intermediate state dynamics is much faster than that of t_{2g} orbitals we are interested in, and thus regard the matrix elements as phenomenological constants. Further, using that $\mathcal{M}_\Gamma$ does not depend on any coordinate and therefore must be invariant under the octahedral group, we obtain

$$\mathcal{M}_Q \equiv \mathcal{M}_{Q_x} = \mathcal{M}_{Q_z} \tag{5.54}$$

$$\mathcal{M}_T \equiv \mathcal{M}_{T_x} = \mathcal{M}_{T_y} = \mathcal{M}_{T_z} \tag{5.55}$$

$$\mathcal{M}_l \equiv \mathcal{M}_{l_x} = \mathcal{M}_{l_y} = \mathcal{M}_{l_z}. \tag{5.56}$$

The $\mathcal{M}_\Gamma$ are hard to calculate explicitly since they involve inverting H, which contains the multiplet structure. In the following, we assume $\mathcal{M}_\Gamma = \mathcal{M}$ for all Γ. This is a reasonable assumption: the core hole generates a multitude of many-body states that evolves very rapidly due to the large spin-orbit coupling and intra-ionic Coulomb interactions, and therefore its potential is averaged. Any particular symmetry is washed away; all become equal, except for the A_{1g} component, which is enhanced at the cost of the others. This is also the reason why the experiments at the t_{2g} and e_g edges are similar [202]: the different edges create different multiplet structures initially, but these differences are averaged out by the intermediate state dynamics, as far as we are concerned with t_{2g} orbital transitions at relatively low energies 0.2-0.3 eV.

Note that P_Γ and $\mathcal{M}_\Gamma$ are independent of the site i. Only $\hat{\Gamma}$ depends on i, giving

$$\hat{O}_{\mathbf{q}} = \sum_\Gamma P_\Gamma \mathcal{M}_\Gamma \sum_i e^{i\mathbf{q}\cdot\mathbf{R}_i} \hat{\Gamma}_i. \tag{5.57}$$

Most interference terms between different Γ's are zero. This comes about because of the specific ground state ordering. Transforming to the local axes (Eq. (15) in Ref. [185]), the ground state and $\hat{H}_0$ are invariant under translations, while the operators $\hat{T}_{\alpha,i}$ and $\hat{l}_{\alpha,i}$ (with $\alpha \in \{x, y, z\}$) acquire a phase upon translation to a different sublattice, which is equivalent to a momentum shift (by orbital ordering vectors) for the corresponding $\hat{\Gamma}_{\mathbf{q}}$. Therefore, many interference terms are zero, which can be seen from Eqs. (5.36) and (5.37): two operators with different momenta cannot bring the ground state (zero momentum) back to itself. The only non-vanishing interference terms are $\langle 0| \hat{Q}^\dagger_{x,\mathbf{q}}(t) \hat{Q}_{z,\mathbf{q}}(0) |0\rangle$ which do not acquire momentum shifts and $\langle 0| \hat{T}^\dagger_{\alpha,\mathbf{q}}(t) \hat{l}_{\alpha,\mathbf{q}}(0) |0\rangle$ where the momentum shifts cancel.

To compare with experiment, we calculate the polarization factors P_Γ for the experimental setup of Ref. [202], where $\mathbf{q}$ is along the [001]-direction. Only

the incoming polarization is fixed, the outgoing polarization is not detected and should be averaged over. We have

$$\boldsymbol{\epsilon} = (\frac{1}{\sqrt{2}}\sin\theta, \frac{1}{\sqrt{2}}\sin\theta, \cos\theta) \tag{5.58}$$

$$\boldsymbol{\epsilon}'_H = (-\frac{1}{\sqrt{2}}\sin\theta, -\frac{1}{\sqrt{2}}\sin\theta, \cos\theta) \tag{5.59}$$

$$\boldsymbol{\epsilon}'_V = (\frac{1}{\sqrt{2}}, \frac{1}{\sqrt{2}}, 0) \tag{5.60}$$

with 2θ the scattering angle. Then, we find for the horizontal outgoing polarization $\boldsymbol{\epsilon}'_H$ (i.e. the electric field vector is in the scattering plane):

$$P_{Q_x,H} = P_{T_x,H} = P_{T_y,H} = P_{l_z,H} = 0 \tag{5.61}$$

$$P_{A_{1g},H} = \frac{1}{3}\cos 2\theta \tag{5.62}$$

$$P_{Q_z,H} = \frac{1}{2\sqrt{3}}(1+\cos^2\theta) \tag{5.63}$$

$$P_{T_z,H} = \frac{1}{2}\sin^2\theta \tag{5.64}$$

$$P_{l_x,H} = -P_{l_y,H} = -\frac{i}{\sqrt{2}}\sin\theta\cos\theta \tag{5.65}$$

and for vertical outgoing polarization $\boldsymbol{\epsilon}'_V$ (electric field vector perpendicular to the scattering plane):

$$P_{A_{1g},V} = P_{Q_z,V} = P_{T_z,V} = 0 \tag{5.66}$$

$$P_{Q_x,V} = -\frac{1}{2}\sin\theta \tag{5.67}$$

$$P_{T_x,V} = -P_{T_y,V} = \frac{1}{2\sqrt{2}}\cos\theta \tag{5.68}$$

$$P_{l_x,V} = P_{l_y,V} = -\frac{i}{2\sqrt{2}}\cos\theta \tag{5.69}$$

$$P_{l_z,V} = \frac{i}{2}\sin\theta. \tag{5.70}$$

For horizontal polarization, the polarization factors make all remaining interference terms zero.

In Appendix B.3, the one- and two-orbiton parts of the $\hat{\Gamma}_{\mathbf{q}} = \sum_i e^{i\mathbf{q}\cdot\mathbf{R}_i}\hat{\Gamma}_i$ are listed. They are obtained by performing the transformations on the orbital operators mentioned in Ref. [185]. Then, the ψ_c orbital (with corresponding annihilation operator $\tilde{c}$) is condensed:

$$n_{\tilde{c}} = |c_0|^2 + \delta n_{\tilde{c}} \tag{5.71}$$

where $\delta n_{\tilde{c}}$ is the fluctuating part. In the completely ordered state, $\langle \delta n_{\tilde{c}} \rangle = \langle n_{\tilde{a}} \rangle = \langle n_{\tilde{b}} \rangle = 0$ and $|c_0|^2 = 1$, while in the completely disordered state $\langle \delta n_{\tilde{c}} \rangle = \langle n_{\tilde{a}} \rangle = \langle n_{\tilde{b}} \rangle = 1/3$ and $|c_0|^2 = 0$. Ref. [185] obtains a finite value for the quadrupole orbital order parameter:

$$\hat{Q} = n_{\tilde{c}} - (n_{\tilde{a}} + n_{\tilde{b}})/2 \equiv \left\langle \hat{Q} \right\rangle + \delta\hat{Q} \simeq 0.19 + \delta\hat{Q} \tag{5.72}$$

with the fluctuating part averaging to zero. This fixes $|c_0|^2 \simeq 0.19$. Taking the square root of Eq. (5.71), one arrives at

$$\tilde{c} = \tilde{c}^\dagger = \sqrt{|c_0|^2 + \delta n_{\tilde{c}}} \approx |c_0| + \frac{1}{2\,|c_0|}\delta n_{\tilde{c}} \tag{5.73}$$

to first order in the fluctuations $\delta n_{\tilde{c}}$.

In the process of writing the $\hat{\Gamma}_{\mathbf{q}}$ in terms of orbiton operators, unphysical contributions to the intensity may appear as a result of neglecting cubic and higher order terms in the orbiton operators. When restoring all terms, these unphysical contributions should cancel by symmetry. For $\mathbf{q}$ along the [001] direction for instance, $[\hat{H}, \hat{Q}_{z,\mathbf{q}}] = 0$ if we use the untransformed forms Eqs. (5.7) and (B.5), and it is clear that there should only be an elastic contribution to the intensity. However, in terms of orbitons, this selection rule is violated if we go only up to quadratic orbiton terms. To make sure these unphysical contributions are dropped, we first calculate the commutator in the untransformed picture. If this yields zero, the commuting part of the scattering operator is dropped. Applying this procedure to the case where $\mathbf{q}$ is along the [001] direction, we find that only $\hat{Q}_{z,\mathbf{q}}$ among the operators (5.43) to (5.45) is zero while all the other channels give finite contributions.

Since we did not include explicitly the orbiton-orbiton interactions, damping of the orbitons should still be taken care of, at least on a phenomenological level. As in the case of Raman scattering calculations, we introduce by hand an energy broadening γ of the orbiton states (half-width at half maximum, HWHM) of $\gamma = 0.4\ J_{\mathrm{orb}}$. This broadening can also be used to take orbiton damping by phonons, magnons etc. into account. In addition to this, there is an experimental broadening added of 27.5 meV (HWHM) [202].

The resulting spectra are shown in Fig. 5.7. The intensity is strongly momentum-dependent (especially for $\mathbf{q}$ along the z direction), which is also seen in the experiments [202]. This dependence is mainly due to the coherent response of the exchange-coupled orbitals which enhances at large momenta, reflecting staggered orbital order in the ground state – Eq. (5.9). In Fig. 5.8, the theoretical cross section (with $\mathbf{q}$ along the z direction and horizontal incoming polarization, i.e. the electric field is in the scattering plane) is compared to the experimental data. The main features of the data [202] are reproduced: the spectral weight increases with increasing q_z and there is virtually no dispersion of the maximum of the theoretical curve (because it is determined by the two-orbiton continuum, containing an integration over the Brillouin zone).

Especially in plots (b) and (c), the one-orbiton shoulder seems a bit too large. We note here again that the weight of this shoulder is controlled by the orbital order parameter: if the orbital order melts, $|c_0|^2$ decreases and the one-orbiton peak becomes less intense. The value we used ($|c_0|^2 = 0.19$) is obtained at zero temperature, assuming that $YTiO_3$ is a fully saturated ferromagnet [184, 185]. Under realistic conditions, $|c_0|^2$ is expected to be smaller than 0.19. Indeed, the saturated ordered moment in $YTiO_3$ is actually $0.84\mu_B$, which is reduced further to approximately $0.80\mu_B$ at $T = 15$ K [203, 210]. Correspondingly, the orbital order is decreased by joint spin-orbital quantum fluctuations, suppressing the one-orbiton peak.

The best chance to see a one-orbiton contribution to the spectrum is with momentum transfer directed maximally in the [110] direction. Fig. 5.9 shows the prediction for the shakeup mechanism with $|c_0|^2 = 0.19$: the one-orbiton peak is about as strong as the two-orbiton peak.

Single site processes – Local model. Although the response functions of the local model of $YTiO_3$ are entirely different from the superexchange model, the phenomenological scattering operator Eq. (5.1) is still valid. Focusing on single site processes, Eq. (5.57) can be evaluated using the wave functions found by Pavarini *et al.*: Eqs. (5.11) through (5.13). Since the eigenstates of the local model have a very simple form, we can straightforwardly use Eqs. (B.1) through (B.8) to evaluate the RIXS spectrum. The P_Γ and $\mathcal{M}_\Gamma$ remain the same as in the collective orbiton case. The spectrum now consists of two sharp peaks at ω_1 and ω_2. These peaks can be broadened by coupling to the lattice as well as due to the SE coupling.

Because there are four sublattices which all support their own, local eigenstates, the RIXS intensity can be decomposed into four signals. From the expressions Eqs. (5.18) through (5.21), it is easily derived how the $\hat{\Gamma}_i$ transform.

So far, the analysis is similar to Sec. 5.4.4. However, in the local model, the eigenstates are local and this changes the analysis of Sec. 5.4.4 at two important points. The first one is that the momentum shifts of $\hat{\Gamma}_{\mathbf{q}}$ do not destroy interference terms: any final state $|f\rangle$ can be reached with any shift of $\mathbf{q}$. All interference terms can in principle be present. The second point to be noted is that, because the eigenstates are local, the only momentum dependence of the cross section comes in through the experimental geometry, which is reflected in the polarization factors P_Γ.

When we compare the theoretical RIXS spectrum of this model to experiment, we again have to take into account the average over the two outgoing polarizations. Assuming again $\mathcal{M}_\Gamma$ are the same for all Γ, and introducing the same broadening as before (HWHM $\gamma \approx 30$ meV phenomenological intrinsic broadening plus 27.5 meV HWHM experimental broadening), we obtain the spectra shown by the solid lines in Fig. 5.10.

It is evident that the local model yields a RIXS spectrum that does not agree

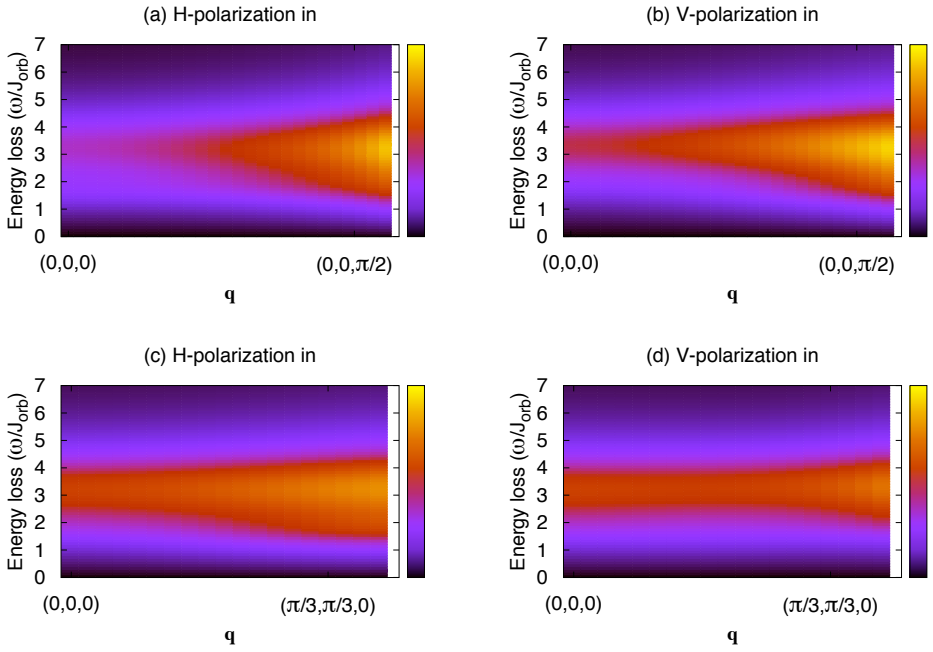

Figure 5.7: RIXS spectra for a model of superexchange-driven orbital order with RIXS coupling to orbitons only via the single site mechanism. Spectra (a) and (b) are for $\mathbf{q}$ directed along the [001] direction, and (c) and (d) for $\mathbf{q}$ along the [110] direction. Spectra (a) and (c) are for horizontal incoming polarization (electric field in the scattering plane), and (b) and (d) are for vertical incoming polarization (electric field perpendicular to the scattering plane). Note that the $\mathbf{q} = \mathbf{0}$ points are different in each spectrum because of the different experimental geometries, leading to different P_Γ. We only plotted the experimentally accessible part of the Brillouin Zone.

well with experiment. Firstly, there is no two-peak structure visible in the data. The presence of a two-peak structure in the theoretical curves does not depend on the assumption that all the $\mathcal{M}_\Gamma$ are equal. We may finetune the model to produce a better fit by changing the energy levels found in Ref. [191] so that both crystal field transitions have an energy of 240 meV, and introducing a very large intrinsic broadening of 100 meV (see the dashed lines in Fig. 5.10). But even in the artificially optimized case of degenerate levels to produce a single peak, the intensity trend remains in contradiction with experiment. Further, it is impossible to tune the energy levels to optimize simultaneously the RIXS and Raman data. Both experiments show a peak at the same energy, while the local model theory predicts the Raman spectra (with its double crystal field excitations) to peak at approximately double the RIXS peak energy.

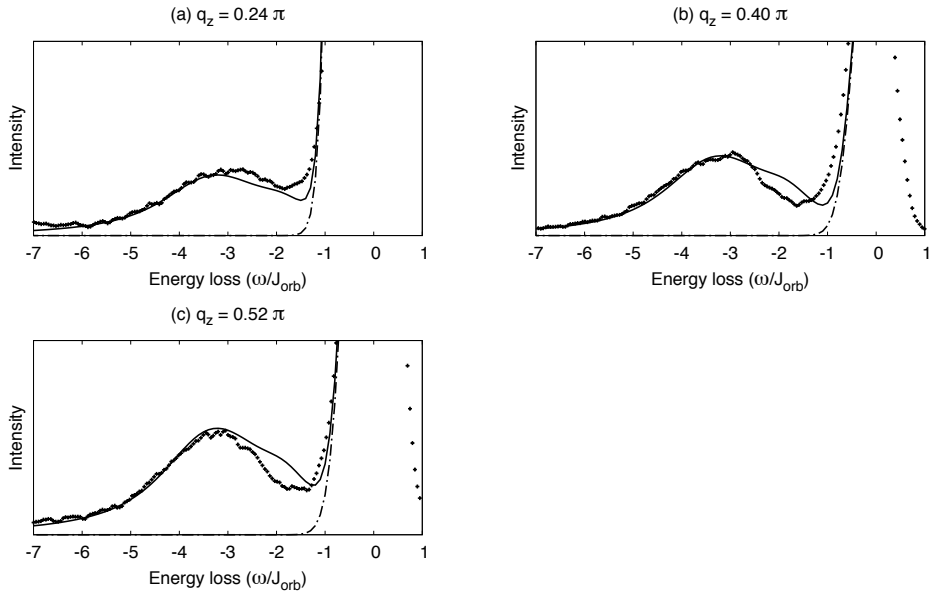

Figure 5.8: RIXS spectra for a SE-driven orbital order with RIXS coupling to orbitons only via the single site mechanism (solid line), compared to the experimental data [202]. The vector $\mathbf{q}$ is directed along the [001] direction, with q_z as indicated in the figures. We took $J_{\rm orb} = 80$ meV, and introduced a phenomenological HWHM broadening of $\gamma = 0.4\ J_{\rm orb} \approx 30$ meV for the orbitons, as well as the HWHM experimental resolution of 27.5 meV. The elastic peak is fitted with a Gaussian (dash-dotted line).

Even though we could improve the line shape by increasing γ, the intensity gain with increasing q_z cannot be reproduced in any way. In fact, the trend is the opposite: as q_z increases, the spectral weight of the theoretical spectrum decreases (see Fig. 5.10). We recall that the $\mathbf{q}$-dependence in this case is merely due to polarization factors Eqs. (5.61−5.70), since in a local picture, each Ti ion contributes independently to the cross section. This is in sharp contrast with the superexchange picture, where the intensity has an intrinsic $\mathbf{q}$-dependence because of the collective response of all the Ti ions.

Two-site processes. The second term in the expansion of the effective scattering operator, Eq. (5.1), involves two-site processes. Due to the strong multiplet effects, the core hole potential is averaged out and becomes mainly of A_{1g} symmetry. While such a potential cannot directly flip the orbitals at the core hole site, it does affect multi-site processes. In the case of the superexchange model, the core hole potential effectively changes the superexchange constant J_{SE} lo-

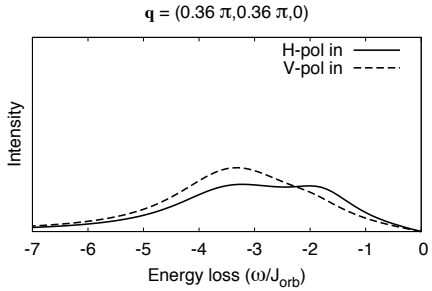

Figure 5.9: Spectra, obtained with the single site mechanism, for the largest experimentally accessible momentum transfer directed along the [110] direction. The solid line indicates the case where the incoming polarization is horizontal, the dashed line is for vertical incoming polarization. The elastic peak has been removed. In the horizontally polarized case, the single orbiton peak is quite strong and should be visible in experiments if the system is superexchange-driven and the RIXS signal is dominated by the single site mechanism.

cally as discussed earlier in the context of RIXS on magnons [10, 51, 52]. This process is illustrated in Fig. 5.11. (In principle, it is also possible that the core hole potential modifies the orbital interactions via the lattice vibrations.) In this section, we consider the superexchange modulation mechanism to illustrate two-site process in RIXS on orbital fluctuations.

The SE modification can be derived explicitly by starting from a Hubbard model

$$\begin{aligned}\tilde{H} = &- t\sum_i \left(b^\dagger_{i\pm\hat{x}}b_i + c^\dagger_{i\pm\hat{x}}c_i + a^\dagger_{i\pm\hat{y}}a_i + c^\dagger_{i\pm\hat{y}}c_i + a^\dagger_{i\pm\hat{z}}a_i + b^\dagger_{i\pm\hat{z}}b_i\right)\\ &+ U\sum_i \left(n_{b,i}n_{c,i} + n_{a,i}n_{c,i} + n_{a,i}n_{b,i}\right)\\ &- U_c\sum_i p_i p_i^\dagger \left(n_{a,i} + n_{b,i} + n_{c,i} - 1\right)\end{aligned} \tag{5.74}$$

where the last term includes the Coulomb energy U_c of the core hole attracting the t_{2g} electrons. p_i is the annihilation operator for 2p core electrons at site i. We have taken the core hole potential to be of A_{1g} symmetry. Doing perturbation theory to second order in $t/U_{(c)}$ (U and U_c are about the same order of magnitude), we obtain the superexchange Hamiltonian

$$H = H_0 + \sum_{i,\delta} p_i p_i^\dagger \left(J_2\hat{A}^{(\gamma)}_{i,i+\delta} - J_1\hat{n}^{(\gamma)}_{i+\delta} + \text{const.}\right) \tag{5.75}$$

with δ pointing to nearest neighbors, $n^{(c)}_i = n_{a,i} + n_{b,i}$ (the other $n^{(\gamma)}$ can be

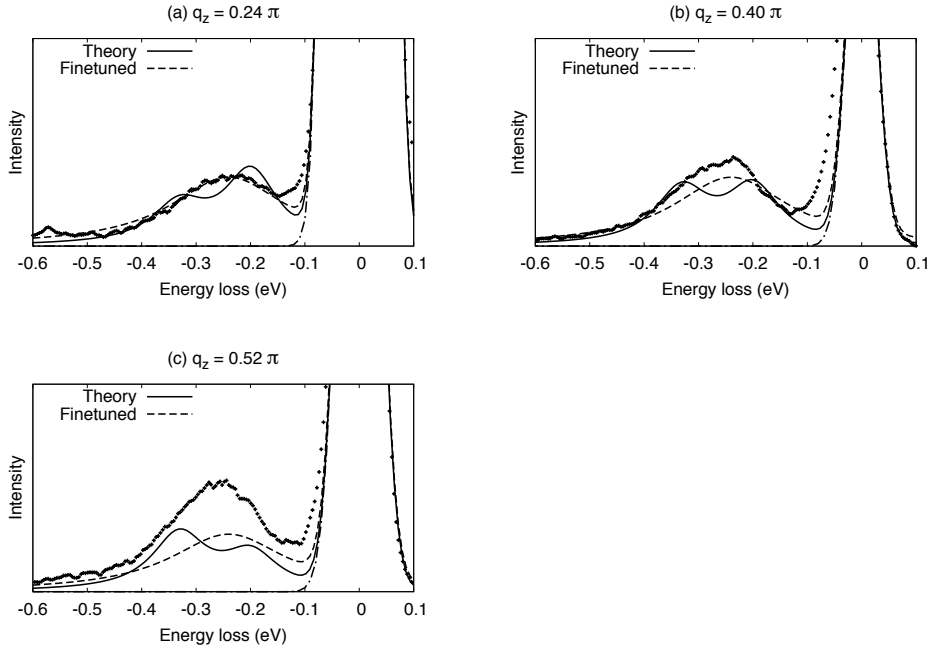

Figure 5.10: RIXS spectra for the local model (solid and dashed lines) compared to experimental data [202]. The vector $\mathbf{q}$ is directed along the [001] direction, where q_z is indicated in the figures. The dashed curve shows the artificially optimized model with degenerate crystal field levels. We introduced a phenomenological intrinsic HWHM broadening ($\gamma \approx 30$ meV [solid line] and $\gamma = 100$ meV [dashed line]) for the final states and added experimental broadening.

obtained by permuting the indices a, b, c) and

$$J_1 = \frac{t^2}{U - U_c} - \frac{t^2}{U} \qquad \text{and} \qquad J_2 = \frac{t^2}{U + U_c} + \frac{t^2}{U - U_c} - \frac{2t^2}{U} \tag{5.76}$$

so that $J_1/J_2 = (1 + U/U_c)/2$. Eq. (5.75) shows we get the unperturbed Hamiltonian plus a contribution which is active only if there is a core hole (in which case $p_i p_i^\dagger \to 1$). The J_1 term involves single site processes only, and is therefore included in the general description in Sec. 5.4.4. In the following, the J_1 term will be dropped.

For simplicity, polarization effects are neglected and we assume U_c to be independent of the specific dipole transition. We take

$$\hat{D} = \sum_i \left(e^{-i\mathbf{q}_{\rm in}\cdot\mathbf{R}_i} p_i d_i^\dagger + e^{i\mathbf{q}_{\rm out}\cdot\mathbf{R}_i} p_i^\dagger d_i \right) + \text{h.c.} \tag{5.77}$$

with p_i the 2p electron annihilation operator and d_i the 3d e_g electron annihilation

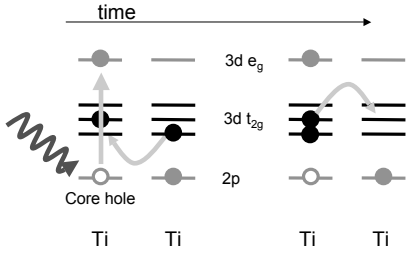

Figure 5.11: In the SE model, two-site RIXS processes locally modify the SE interaction, coupling the RIXS core hole to the t_{2g} orbitals. Shown is an orbital SE process between two neighboring Ti ions in the presence of a core hole. On the left, one of the ions is excited by an incoming x-ray photon. After that, the t_{2g} electrons undergo a SE process. On the right, the virtual state of the SE process is depicted. The presence of the core hole frustrates the SE process. Instead of the usual Hubbard U, the energy of the virtual state is lowered by the presence of the positively charged core hole. This modifies the SE constant $J_{SE} = 4t^2/U$ at the core hole site.

operator. The position of the i^{th} site is $\mathbf{R}_i$. The transfered momentum is $\mathbf{q} = \mathbf{q}_{\text{out}} - \mathbf{q}_{\text{in}}$. The neglected polarization dependence could give rise to a $\mathbf{q}$-dependent factor in the cross section, but will not affect the line shape for a specific $\mathbf{q}$.

The relevant energy scale for the excitation of orbitons in the intermediate states via superexchange bond modulation is J_2, as established above, as long as the core hole potential is of A_{1g} symmetry. This is the case when core level spin-orbit coupling and Hund's rule coupling are large compared to J_2: the core hole evolves rapidly with time and its potential's symmetry averages out to A_{1g} before any orbitons can be excited. Because the symmetry is effectively cubic, bonds in all directions are affected in the same way. The effective scattering operator must therefore be a function of $\sum_\delta \hat{A}^{(\gamma)}_{i,i+\delta}$ which is of A_{1g} symmetry. Non-linear operators like $\hat{A}^{(\gamma)}_{i,i+\delta}\hat{A}^{(\gamma)}_{i,i+\delta'}$ are excluded, they are expected to yield smaller contributions because more and more distant sites are involved. In the expansion Eq. (5.1), these come in at different orders. The only remaining candidate for the two-site effective scattering operator is therefore

$$\hat{O}_{\mathbf{q}} = \mathcal{M}_2 \sum_{i,\delta} e^{i\mathbf{q}\cdot\mathbf{R}_i} \hat{A}^{(\gamma)}_{i,i+\delta} \tag{5.78}$$

where $\mathcal{M}_2$ is an unknown phenomenological matrix element, in the same way as in Sec. 5.4.4. By construction, the two-site process matrix element $\mathcal{M}_2$ should be proportional to J_2 with a constant determined by the intermediate state dynamical susceptibilities. At this stage, without microscopical calculations of the single-site $\mathcal{M}_\Gamma$ (5.52) and two-site $\mathcal{M}_2$ matrix elements, we cannot judge which

coupling process dominates the observed RIXS on orbital excitations. Instead, we calculate two-site process independently and compare it with both experimental data and the results obtained above for single-site coupling mechanism.

As it turns out, the two-site effective scattering operator (5.78) contains only two-orbiton creation terms; it does not create single orbitons because the orbitons are constructed in the first place to diagonalize the Hamiltonian: all linear contributions to $\hat{A}_{ij}^{(\gamma)}$ in Eq. (5.8) are canceled (similar to the Raman scattering calculations above).

Using again the transformations on the orbital operators mentioned in Ref. [185], condensing the ψ_c orbital and transforming to orbiton operators, we obtain for the two-orbiton creation part

$$\begin{aligned}\hat{O}_{\mathbf{q}}^{(2)} =& \mathcal{M}_2 \sum_{\mathbf{k}} \Big[f_{11}(\mathbf{k},\mathbf{q}) \alpha_{1,\mathbf{k}}^{\dagger} \alpha_{1,-\mathbf{k}-\mathbf{q}}^{\dagger} \\ &+ f_{22}(\mathbf{k},\mathbf{q}) \alpha_{2,\mathbf{k}}^{\dagger} \alpha_{2,-\mathbf{k}-\mathbf{q}}^{\dagger} + f_{12}(\mathbf{k},\mathbf{q}) \alpha_{1,\mathbf{k}}^{\dagger} \alpha_{2,-\mathbf{k}-\mathbf{q}}^{\dagger} \Big] \end{aligned} \tag{5.79}$$

where the $f_{ij}(\mathbf{k},\mathbf{q})$ are lengthy functions listed in Appendix B.4. The cross section then is

$$\begin{aligned}\frac{d^2\sigma^{(2)}}{d\omega d\Omega} &\propto \sum_f \left| \langle f | \, \hat{O}_{\mathbf{q}}^{(2)} \, |0\rangle \right|^2 \delta(\omega - \omega_{1/2,\mathbf{k}} - \omega_{1/2,\mathbf{k}+\mathbf{q}}) \\ &= \frac{1}{2} \sum_{\mathbf{k}} \Big[\left| f_{11}(\mathbf{k},\mathbf{q}) + f_{11}(-\mathbf{k}-\mathbf{q},\mathbf{q}) \right|^2 \delta(\omega - \omega_{1,\mathbf{k}} - \omega_{1,\mathbf{k}+\mathbf{q}}) \\ &+ \left| f_{22}(\mathbf{k},\mathbf{q}) + f_{22}(-\mathbf{k}-\mathbf{q},\mathbf{q}) \right|^2 \delta(\omega - \omega_{2,\mathbf{k}} - \omega_{2,\mathbf{k}+\mathbf{q}}) \\ &+ 2 \left| f_{12}(\mathbf{k},\mathbf{q}) \right|^2 \delta(\omega - \omega_{1,\mathbf{k}} - \omega_{2,\mathbf{k}+\mathbf{q}}) \Big] . \end{aligned} \tag{5.80}$$

The resulting cross section for transfered momenta along the [001] direction is shown in Fig. 5.12. As in the above sections, we introduced here by hand an energy broadening γ of the orbiton states of $\gamma = 0.4\, J_{\mathrm{orb}}$.

A few things should be noted. Firstly, the spectrum disappears at $\mathbf{q} = \mathbf{0}$. This is clear from Eq. (5.78): the scattering operator becomes proportional to the Hamiltonian Eq. (5.7), giving elastic scattering only.

Secondly, the spectrum shown in Fig. 5.12 is calculated without taking polarization dependence into account. That could change the relative spectral weight for different $\mathbf{q}$'s, but does not affect the line shapes.

In Fig. 5.13 we compare the calculated superexchange spectra for the specific $\mathbf{q}$ values of the experiments reported in Ref. [202]. The only free parameter (J_{orb}) gives a best fit for $J_{\mathrm{orb}} = 75$ meV. As is evident, the increase in spectral weight is qualitatively accounted for by the theory, although the theoretical curves show a much stronger increase with increasing q_z. We note that one factor that could diminish this discrepancy is, as stated above, the polarization factor we omitted: it could change the relative weight (but not the line shape).

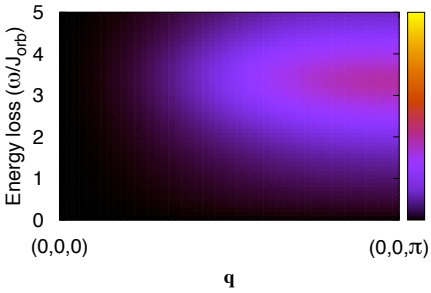

Figure 5.12: RIXS spectrum for two-site processes within the superexchange model. The color scale denotes the intensity. The figure shows $\mathbf{q}$ running from $(0,0,0)$ to $(0,0,\pi)$. One-orbiton creation is not allowed for the superexchange modulation mechanism. The intrinsic energy broadening γ of the orbiton states is $\gamma = 0.4\ J_{\rm orb} \approx 30$ meV, and the added experimental resolution of 27.5 meV [202] is approximately $0.34\ J_{\rm orb}$.

Summarizing, two-site processes can capture some of the features seen in the RIXS data (the intensity trend with increasing momentum transfer, and a single peak without dispersion), but the overall fit is less satisfactory compared to the results of the single-site process shown in Fig. 5.8.

5.4.5 Conclusions

We have considered two different models, widely discussed in literature to describe orbital physics in titanites, in the context of Raman and X-ray scattering experiments. These models correspond to two limiting cases where the orbital ground state is dominated either by collective superexchange interactions among orbitals or by their coupling to lattice distortions. The models predictions, obtained within the same level of approximations, are compared to the experimental data on Raman (Fig. 5.6) and on X-ray (Figs. 5.8 and 5.10) scattering in titanites. What is evident from this comparison and our detailed analysis is that the local crystal field model of $YTiO_3$ fails to give a coherent explanation of both Raman and RIXS data taken together. There is no way one can get rid of the two-peak structure predicted for RIXS by this model without artificially finetuning its parameters. Further, once tuned to the RIXS spectra, the Raman spectra will be impossible to fit with the local model anyway, since it yields double dd excitations, different from the single crystal field excitations in RIXS. Experimentally, however, both techniques show a peak at the same energy. Also, a huge anisotropy between out-of-plane and in-plane polarizations is predicted by the local model, which is not observed in Raman data. Further, the temperature dependence of the experimental data is hard to explain from a local model: the intensity of crystal field transitions is expected to remain unchanged. Finally,

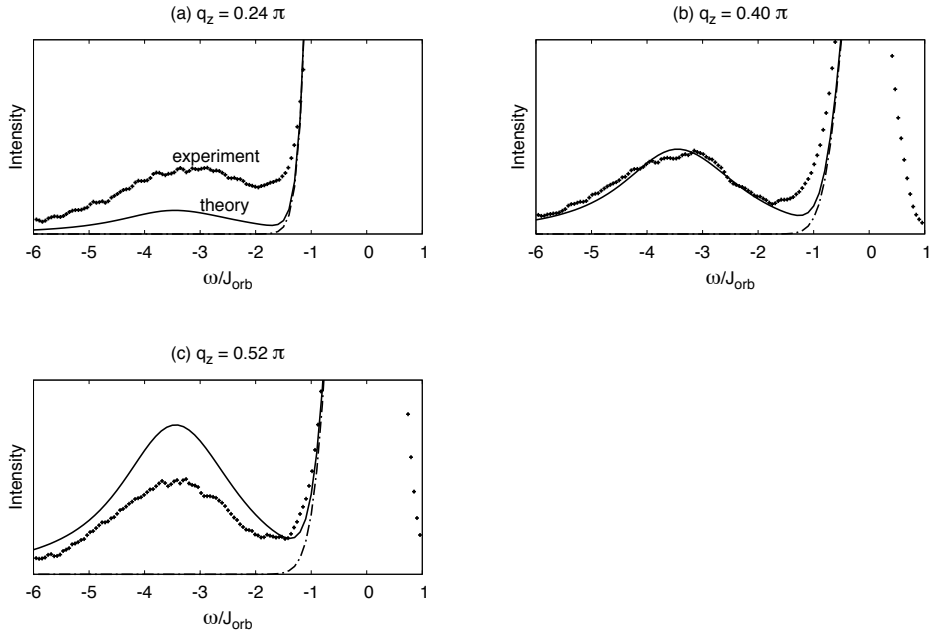

Figure 5.13: Theoretical RIXS spectra for two-site processes, calculated within the superexchange model (solid line), compared to experiment [202]. **q** is directed along the [001] direction, with q_z as indicated. We obtain a best fit for $J_{\rm orb} = 75$ meV. The solid lines are cuts from the plot of Fig. 5.12, where we added a Gaussian fit to the elastic peak (dash-dotted line). A phenomenological intrinsic orbiton broadening of $0.4\, r_1 J_{SE} \approx 30$ meV is added, as well as the experimental resolution of 27.5 meV (both HWHM) [202].

the **q** dependence of the RIXS intensity is not reproduced by the local model; in fact, the trend is opposite. We believe especially the last four points are robust evidence that the 250 meV peak seen in Raman and RIXS is not due to local *dd* excitations.

On the other side, the picture of collective excitations offers much better and broad agreement with the experimental data. The general features of both the Raman and RIXS data are reproduced by the SE model. For RIXS we presented a phenomenological scattering operator for single and two-site processes, evaluated within the SE model. Although both single and two-site processes get the general trends of the RIXS data right, the two-site processes clearly have a too strong **q**-dependence of the intensity. The RIXS spectra obtained with the single site operator fit the data very well, suggesting that this process of generating orbitons might be the predominant one in the transition metal oxides. The only slight deviation from the experiments is the one-orbiton peak, which our theory

overestimates. However, we note that the theoretical one-orbiton peak is decreased if we consider realistic conditions such as finite temperature and residual spin-orbital quantum fluctuations, which obstruct the orbital order and reduce $|c_0|^2$, which in its turn controls the one-orbiton spectral weight.

Ref. [202] reported that the RIXS-intensities in $LaTiO_3$ and $YTiO_3$ show different $\mathbf{q}$ dependences: While the intensity in $YTiO_3$ increases with $\mathbf{q}$, it decreases in $LaTiO_3$. On a qualitative level, this contrasting behavior can be understood from the SE picture as a manifestation of the (dynamical) Goodenough-Kanamori rules, according to which the spin and orbital correlations are complementary to each other. This implies that the spin and orbital susceptibilities are expected to behave in an opposite fashion. Since magnetic orderings in $YTiO_3$ and $LaTiO_3$ are different (ferro- and antiferromagnetic, respectively), collective response of orbitals in these coupounds are expected to be enhanced also at different portions of the Brillouin zone: at large $\mathbf{q}$ in $YTiO_3$ and, in contrast, at small $\mathbf{q}$ in $LaTiO_3$, which are complementary to the respective locations of their magnetic Bragg peaks. The SE picture suggests also that the $\mathbf{q}$-dependence of the orbiton RIXS-intensity should have cubic symmetry in both $LaTiO_3$ and $YTiO_3$, as follows from their isotropic spin-wave [186, 209] and Raman spectra [200]. Future RIXS experiments in titanites would be useful to verify these expectations.

A previous estimate [185] from neutron spin wave data [209] puts the orbital exchange constant $J_{\rm orb}$ at 60 meV. In close agreement with this estimate, the theoretical Raman spectrum fits best to experiment when $J_{\rm orb} = 65$ meV (vertex corrections may change this number, though). Matching to a lesser degree to the estimate, we find for the RIXS spectra $J_{\rm orb} = 75$ and 80 meV for the two-site and single site processes, respectively.

To establish the nature of the 250 meV peak, it is of great importance to search for the one-orbiton peak. In Raman scattering one-orbiton creation seems to be strongly suppressed, but in RIXS it would be possible to see a one-orbiton peak when $\mathbf{q}$ is directed maximally along the [110] direction. There the one-orbiton peak (around $\omega \approx 1.8\ J_{\rm orb} \approx 140$ meV) is about as strong as the two-orbiton continuum, assuming single site processes are the dominant RIXS channel, and provided $|c_0|^2$ is not too small.

To summarize, we may conclude that the existing Raman and RIXS data in titanites are better described by the SE model. This implies that while some polarization of orbitals by static lattice distortions must be a part of a realistic, "ultimate" model for titanites, the orbital fluctuations which are intrinsic to the t_{2g} orbital SE process [187] are not yet suppressed and strong enough to stabilize nearly isotropic charge distributions around the Ti-ions.

On the technical side, we believe that our semi-phenomenological approach to the RIXS problem which disentangles the high energy intermediate state dynamics from low energy collective excitations of orbitals and spins may serve as a simple and efficient tool in the theoretical description of Resonant Inelastic X-ray Scattering in oxides in general.

5.4.6 Acknowledgements

We would like to thank J. van den Brink for stimulating discussions that initiated this work. We also thank B. Keimer, C. Ulrich, and M. W. Haverkort for many fruitful discussions. L. A. thanks the Max-Planck-Institut FKF, Stuttgart, where most of the work was done, for its hospitality.